

Optical and electro-optical properties
of BaTiO₃ thin films and
Mach-Zehnder waveguide modulators

von

Adrian Ion Petraru

Optical and electro-optical properties of BaTiO_3 thin films and Mach-Zehnder waveguide modulators

Inaugural-Dissertation
zur
Erlangung des Doktorgrades
der Mathematisch-Naturwissenschaftlichen Fakultät
der Universität zu Köln

vorgelegt von
Adrian Ion Petraru
aus Braila

Forschungszentrum Jülich

2003

Berichterstatter: Prof. Dr. Ch. Buchal
Prof. Dr. L. Bohatý

Tag der mündlichen Prüfung: 10.11.2003

Zusammenfassung

Die vorliegende Dissertation beschreibt die Herstellung und Charakterisierung von integriert- optischen Wellenleitermodulatoren auf der Basis von BaTiO_3 , wobei in dieser Arbeit zum ersten Mal Monomode- Mach-Zehnder- Modulatoren mit Hilfe der BaTiO_3 - Dünnschichtepitaxie realisiert wurden. Die epitaktischen BaTiO_3 - Filme wurden mit dem Verfahren der gepulsten Laserdeposition (PLD) von einem polykristallinen BaTiO_3 - Target abgetragen und auf einem einkristallinen $\text{MgO}(100)$ - Substrat aufgewachsen. Durch Variation der Wachstumsbedingungen konnte erreicht werden, daß die c-Achse der BaTiO_3 - Schichten senkrecht zur Schichtebene oder aber in der Schichtebene liegend orientiert war. Mit Hilfe eines Prismenkoppelmessplatzes wurden die optischen Indizes und die optische Absorption der BaTiO_3 - Schichten auf $\text{MgO}(100)$ vermessen. Als weitere prinzipielle Charakterisierungsverfahren wurden Röntgenbeugung, Rutherford- Rückstreuung und Ionenchanneling sowie die atomare Kraftmikroskopie eingesetzt. Hochwertige BaTiO_3 - Schichten wurden anschließend mit Hilfe der Lithographie und des Ionenstrahlätzens strukturiert zu verzweigten Monomode- Wellenleitern, die für eine Mach- Zehnder- Modulatoranordnung erforderlich sind. Längs der Wellenleiter wurden lithographisch strukturierte Goldelektroden deponiert. Mit Hilfe eines Wellenleitermessplatzes konnten die elektrooptischen Koeffizienten der BaTiO_3 - Schichten unterschiedlicher kristallographischer Orientierung bestimmt werden. Zusätzlich wurde bei einer Reihe von Experimenten durch Absenken der Substrattemperatur während des PLD- Prozesses die Epitaxie behindert und auf diese Weise polykristallines BaTiO_3 auf MgO abgeschieden. Auch die derart hergestellten polykristallinen BaTiO_3 - Schichten konnten für Mach- Zehnder- Modulatoren eingesetzt werden. Ihre reduzierten "effektiven" elektrooptischen Koeffizienten wurden bestimmt.

Abstract

The rapidly developing field of communication has increased the interest for electro-optic devices based on ferroelectric thin films and for their integration with silicon or III-V compounds. BaTiO₃ is a representative ferroelectric material which is well suited for optical applications because of its high optical transparency and its large linear and non-linear electro-optic coefficients. Epitaxial BaTiO₃ films on MgO(100) deposited by pulsed laser deposition with c-axis and a-axis orientation are investigated. Because of their potential for integration with silicon, polycrystalline BaTiO₃ thin films are also investigated. For the structural characterization of the films, different techniques like Rutherford backscattering spectrometry/ ion channelling, x-ray diffraction and atomic force microscopy are used. Optical waveguides were patterned by lithography and ion beam etching. The waveguide losses and the refractive indices were measured with a prism coupling setup. Mach-Zehnder waveguide modulators were demonstrated for both epitaxial and polycrystalline films. The electro-optic coefficients for two orientations of the epitaxial grown films (c-axis and a-axis orientation) and for the polycrystalline films were experimentally determined. The modulators could be modelled using the Jones matrix formalism and the effective Pockels coefficients of the epitaxial single crystalline and the polycrystalline BaTiO₃ films are evaluated.

Contents

1	Introduction	1
2	BaTiO₃	3
2.1	The BaTiO ₃ bulk crystal	3
2.2	Crystal structure and phase transitions	3
2.3	Optical properties	5
2.4	Electro-optic coefficients	7
3	Theoretical background	9
3.1	Asymmetric planar dielectric waveguides	9
3.2	Light coupling into the waveguides	10
3.2.1	Direct focussing	10
3.2.2	Prism couplers	11
3.2.3	Grating couplers	11
3.3	Jones matrix formulation	12
3.4	Electro-optic effect of BaTiO ₃	15
3.5	Mach-Zehnder modulators with the applied electrical field perpendicular to the optical axis	17
3.6	Mach-Zehnder modulators with the applied electrical field parallel to the optical axis	21
4	Experimental	25
4.1	Experimental techniques	25
4.1.1	Pulsed laser deposition	25
4.1.2	X-ray diffraction	25
4.1.3	Rutherford backscattering spectrometry	28
4.1.4	Atomic force microscopy	29
4.2	Mach-Zehnder Modulators	30
4.2.1	Device design and fabrication	30
4.2.2	Ridge waveguides	31
4.3	Experimental set-up	36

4.4	Epitaxial BaTiO ₃	42
4.4.1	c-axis films	42
4.4.2	a-axis films	51
4.5	Polycrystalline BaTiO ₃ Mach-Zehnder modulators	57
4.5.1	Film growth and characterization	58
4.5.2	Optical and electro-optical characterization	59
5	Summary	67
	List of Figures	69
	List of Tables	73
	Bibliography	75
	Acknowledgments	81
	List of publications	85
	Curriculum Vitae	87
	Erklärung	89

Chapter 1

Introduction

The expansion of the field of optocommunication has increased the demand for new materials for integrated optical devices. The optical ferroelectrics in the form of highly transparent thin films are promising materials for communication. Many ferroelectric thin film materials, such as BaTiO_3 [1], KNbO_3 [2], LiNbO_3 [3], $(\text{Pb},\text{La})\text{TiO}_3$ [4], $(\text{Na},\text{K})\text{NbO}_3$ [5], $\text{Pb}(\text{Zr},\text{Ti})\text{O}_3$ [6] have been investigated for their optical and waveguiding properties. The realization of thin film electro-optical devices is of strong scientific and technological interest. BaTiO_3 (BTO) is an attractive candidate for thin film electro-optic modulators due to its large electro-optical coefficients [7], its high optical transparency and its favorable growth characteristics.

In chapter 2 a short description of BaTiO_3 is given, including the crystal structure, the phase transitions and the optical and the electro-optical properties of the material. Chapter 3 introduces the concepts of the asymmetric planar dielectric waveguides and different methods of light coupling into the waveguides are discussed. The Jones matrix calculus and the electro-optic effect of BaTiO_3 are briefly presented. A theoretical modelling of Mach-Zehnder waveguide modulators for two particular geometries (electrical field perpendicular and parallel to the optical axis) is given. In the next chapter, the section 4.1 is about the experimental techniques employed for structural, optical and electro-optical characterization of the BaTiO_3 deposited film. A short description of the pulsed laser deposition method is given. The next part (section 4.2) describes the fabrication of the single mode ridge waveguides on BaTiO_3 thin films on MgO and the design and fabrication of Mach-Zehnder modulators. The growth and characterization of the epitaxial BaTiO_3 films on MgO deposited by pulsed laser deposition for two kinds of film orientation (c-axis and a-axis oriented films) is discussed in section 4.4. After demonstrating Mach-Zehnder modulators for both types of epitaxial

films, the evaluation of the effective electro-optic coefficients is presented. In section 4.5 the growth and structural characterization of polycrystalline BaTiO_3 films on MgO is discussed. A Mach-Zehnder modulator based on this type of film is demonstrated. The polycrystalline BaTiO_3 films show useful electro-optic properties and high transparency.

Chapter 2

BaTiO₃

2.1 The BaTiO₃ bulk crystal

Barium titanate (BaTiO₃) was one of the first ferroelectric materials to be discovered, and also one of the first to be recognized as photorefractive [8]. This material is, to date, the most extensively investigated ferroelectric material. BaTiO₃ is a member of the perovskites family, of which the parent member is the mineral CaTiO₃, called perovskite. The perovskite family includes other well-known materials such as KNbO₃, KTaO₃, PbTiO₃ and SrTiO₃. The general formula of compound belonging to this family is ABO_3 , where A is a monovalent, divalent or trivalent metal and B a pentavalent, tetravalent or trivalent element, respectively. From the point of view of practical applications this material is very interesting because it is chemically and mechanically very stable and it exhibits ferroelectric properties [9] at and above room temperature. From the optical applications point of view, BaTiO₃ is very interesting because of its high linear and nonlinear electro-optic coefficients.

2.2 Crystal structure and phase transitions

The Curie temperature of BaTiO₃ is at 120 °C. Above this temperature, BaTiO₃ is paraelectric in the cubic phase (point group $m\bar{3}m$), thus centrosymmetrical. The structure of BaTiO₃ in the cubic phase is a simple one (Fig. 2.2a) with Ba²⁺ ions at the cube corners, Ti⁴⁺ ions at the body centers, and O²⁻ ions at the face centers. Below the Curie temperature BaTiO₃ undergoes a phase transition to the tetragonal phase with the point group $4mm$, and the material becomes ferroelectric. In the tetragonal phase BaTiO₃ is non-centrosymmetric. The most important change in the struc-

ture is a shift of Ti⁴⁺ ion from the center of the octahedron toward an oxygen ion at one of the face centers of the cubic unit cell (Fig. 2.2b). The four-fold rotation axis is thus the polar direction, identified with the tetragonal c axis. The c axis lies parallel to the direction of one of the original cubic $\langle 100 \rangle$ directions. The tetragonal unit cell results from the distorted cubic cell, with one edge elongated to become the tetragonal c axis and the other two cube edges compressed to become the tetragonal a axes. Because there are six equivalent $\langle 100 \rangle$ axes in the cubic phase, the polar axis can be parallel to any of these six equivalent directions, giving rise to complicated domain patterns. The tetragonal phase is stable from 120 °C to about 5 °C. Below 5 °C, the BaTiO₃ phase is orthorhombic with symmetry belonging to the point group mm . This phase is still ferroelectric, but the direction of spontaneous polarization is parallel to one of the original cubic $\langle 110 \rangle$ directions. The orthorhombic phase of BaTiO₃ is stable from 5 °C to about -90 °C. At -90 °C another phase transition occurs and the symmetry changes to rhombohedral. The point group of this phase is $3m$ and the polar axis lies along one of the original cubic $\langle 111 \rangle$ directions. The angle between the rhombohedral axes differs from 90° by 12'.

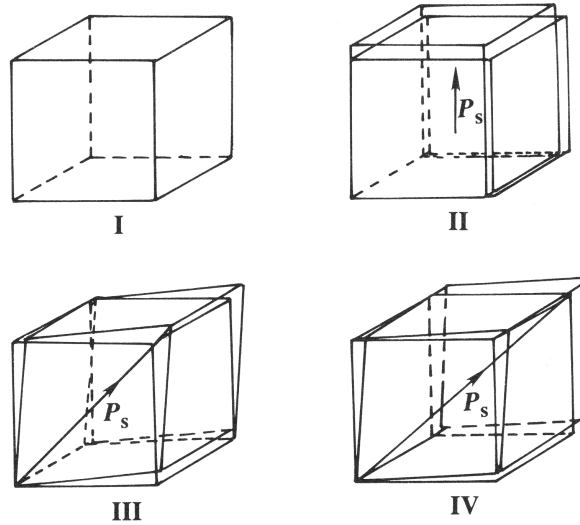
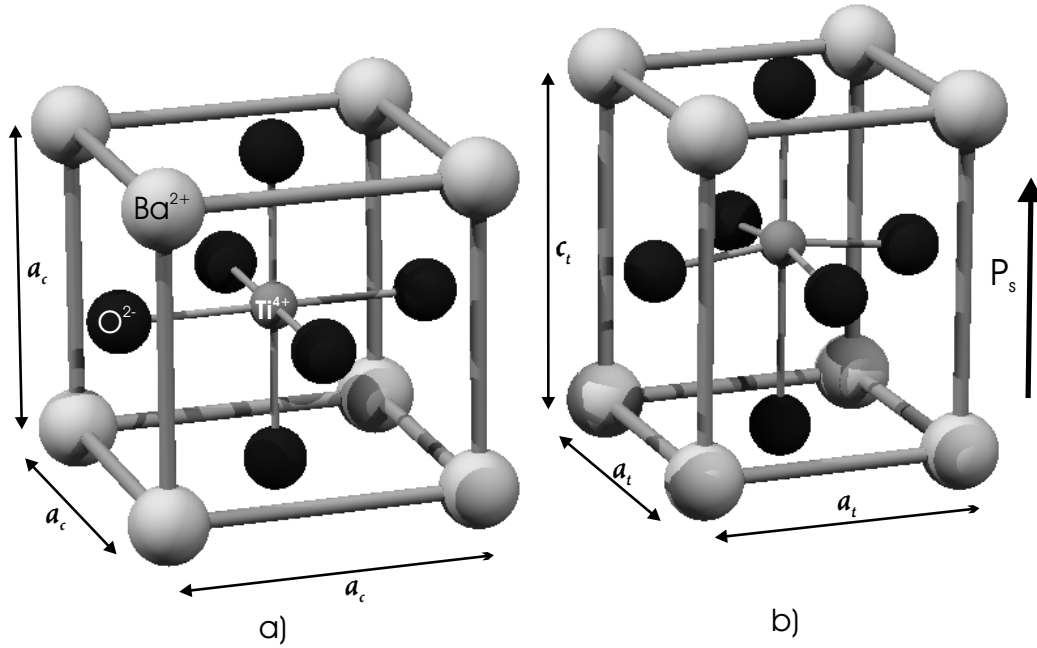


Figure 2.1: Unit cells of the four phases of BaTiO₃.

Figure 2.3 shows the lattice parameters of BaTiO₃ as functions of temperature in the range -150 °C - 150 °C determined by Kay and Vousden on the basis of X-ray diffraction data [10].

The tetragonal phase of BaTiO₃ is of interest for applications because it is stable at room temperature. At 20 °C, the lattice parameters are $c = 4.0361 \text{ \AA}$

Figure 2.2: BaTiO₃ unit cell: a) cubic phase; b) tetragonal phase.

Symmetry	rhombohedral	orthorhombic	tetragonal	cubic
Point group	$3m$	mm	$4mm$	$m3m$
Temperature (°C)	-90			5
Phase	ferroelectric			120
				paraelectric

Table 2.1: The BaTiO₃ phases.

and $a = 3.9920\text{\AA}$ [11]. The tetragonality $t = c/a - 1$ is 1.05% at room temperature.

2.3 Optical properties

BaTiO₃ in its tetragonal phase, at room temperature, is a negative uniaxial crystal with relatively high refractive indices n_o , n_e , if compared with most other solids. The ordinary and extraordinary refractive indices of un-doped BaTiO₃ at 20 °C are $n_o = 2.412$ and $n_e = 2.360$ [11]. The birefringence of the bulk BaTiO₃ crystal is then $\Delta n = n_e - n_o = -0.052$. The temperature dependence of refractive indices is depicted in Fig. 2.4, as measured interferometrically by Hofmann *et al.* [12]. The ordinary refractive index

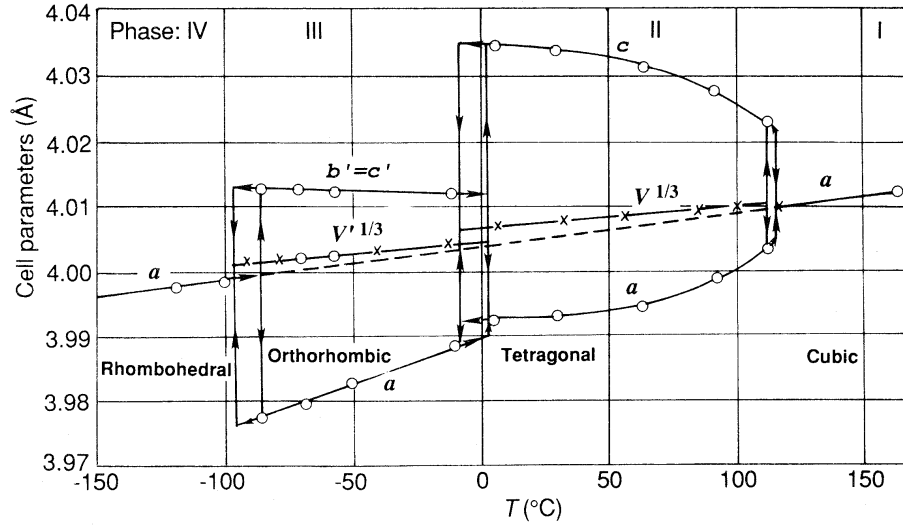


Figure 2.3: Temperature dependence of the cell parameters of BaTiO₃. V is the unit cell volume and b' , c' , V' are cell parameters of the pseudo-cubic unit cell (after Kay and Vousden [10]).

is practically independent of temperature. The temperature derivative of the extraordinary refractive index is $dn_e/dt = 140 \times 10^{-6} \text{ K}^{-1}$ at 514.5 nm wavelength [11].

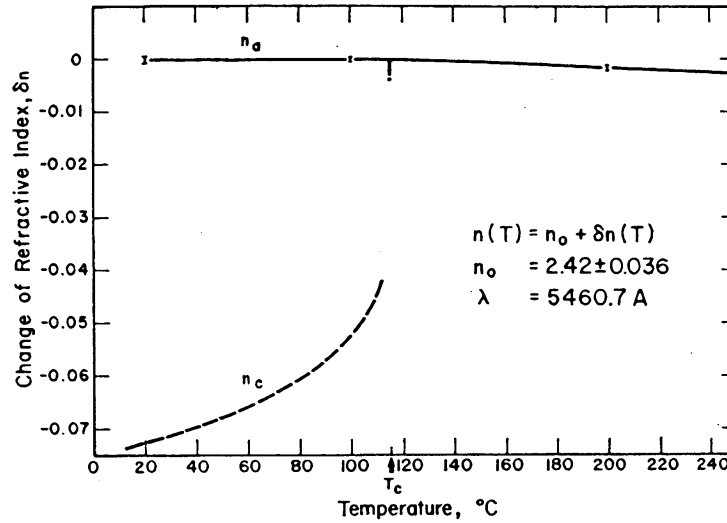


Figure 2.4: Temperature dependence of the refractive indices of BaTiO₃ (after Hofmann *et al.* [12]).

2.4 Electro-optic coefficients

For a BaTiO₃ crystal in its tetragonal phase (point group $4mm$), there are three independent components of the electro-optic tensor: r_{13} , r_{33} and $r_{42} = r_{51}$ (in contracted notation). The unclamped (stress-free) and clamped (strain-free) electro-optic tensors of BaTiO₃ reported by Zgonik *et al.* [7] are given in Table 2.2.

For measuring the unclamped Pockels coefficients, an electric field is applied uniformly throughout an unconstrained sample, and the applied frequencies are below the bulk piezoelectric resonances of the sample, which can range between 1 MHz and 100 MHz.

	r_{13} [pm/V]	r_{33} [pm/V]	r_{42} [pm/V]
Unclamped	8 ± 2	105 ± 10	1300 ± 100
Clamped	10.2 ± 0.6	40.6 ± 2.5	730 ± 100

Table 2.2: Electro-optic coefficients for single crystal BaTiO₃ at 23 °C and $\lambda_0 = 633$ nm.

The clamped conditions correspond to applied frequencies above the piezoelectric resonances. At these high frequencies, all piezoelectric effects are frozen, and thus do not contribute to the electro-optic properties.

The values of the electro-optic coefficients reported by Zgonik are measured at room temperature at 632.8 nm wavelength.

Chapter 3

Theoretical background

3.1 Asymmetric planar dielectric waveguides

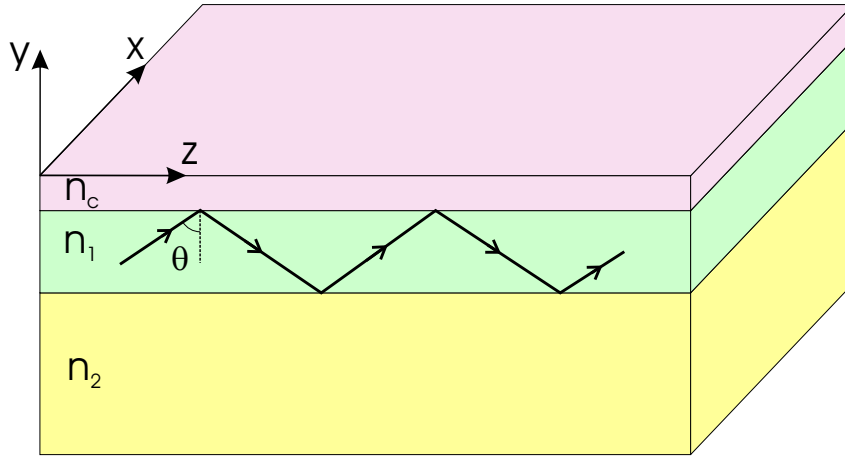


Figure 3.1: Asymmetric planar dielectric waveguide.

A planar dielectric waveguide is a slab of dielectric material surrounded by media of lower refractive indices. The light is guided inside the slab by total internal reflection. In thin film devices the slab is called "film" and the upper and lower media are called the "cladding" and the "substrate", respectively. Light rays making angles θ with the y axis in the y - z plane (Figure 3.1), undergo multiple total internal reflections at the film boundaries if θ is larger than the critical angles $\arcsin(n_c/n_1)$ and $\arcsin(n_2/n_1)$ of the cladding-film and substrate-film interfaces, respectively. Rays making lower θ angles refract, losing a portion of their power at each reflection, and eventually vanish. To determine the waveguide modes, the solution of the Maxwell equations

that match the boundary conditions at the film-substrate and film-cladding interfaces can be found [13]. Another solution to determine the waveguide modes can be found by using the ray optics approach [14, 15, 16]. In the picture of the ray optics, the waveguiding condition imposes that all multiple reflected waves add in phase. The total phase change experienced by the plane wave to travel one round trip, up and down across the film, should be equal to $2m\pi$, where m is an integer. Otherwise, if after the first reflections from the upper and lower film surfaces, the phase of the reflected wave differs from the original wave by a small phase δ , the phase differences after the second, third,..., reflections would be 2δ , 3δ ,..., and then the waves of progressively larger phase differences would be added finally to zero. This condition is expressed by:

$$\begin{aligned} 2dn_1^{TE}k_0 \cos \theta - 2\phi_s^{TE}(\theta) - 2\phi_c^{TE}(\theta) &= 2m\pi \\ 2dn_1^{TM}k_0 \cos \theta - 2\phi_s^{TM}(\theta) - 2\phi_c^{TM}(\theta) &= 2m\pi, \end{aligned} \quad (3.1)$$

where d is the film thickness, $k_0 = 2\pi/\lambda_0$, ϕ_s^{TE} , ϕ_c^{TE} , ϕ_s^{TM} , ϕ_c^{TM} are the Goos-Haenchen shifts due to the total reflection at film-substrate and film-cladding boundaries for the TE and TM polarized waves. The shifts due to the total reflections depend on the angle θ and the polarization. Equation 3.1 is a transcendental equation which can be solved graphically or numerically.

3.2 Light coupling into the waveguides

There are various methods for coupling an optical beam to a waveguide [17]. The coupling efficiency depends strongly on the degree of matching between the profile of the optical beam and that of the waveguide mode.

3.2.1 Direct focussing

The simplest method for coupling a laser beam to a waveguide is the direct focussing or the "end-fire" coupling. The method is especially suited for coupling gas-laser beams (He-Ne laser) to the fundamental waveguide mode because of the relatively good match between the Gaussian beam profile and TE_0 waveguide mode shape. The diameter of the focussed beam must be closely matched to the waveguide thickness for optimum coupling. However, in practice efficiencies about 60% are usually achieved because film thickness is on the order of $1 \mu\text{m}$ and the alignment is very critical. This method is suited for laboratories, the difficulty of maintaining the alignment without an optical bench limits its usefulness in practical applications.

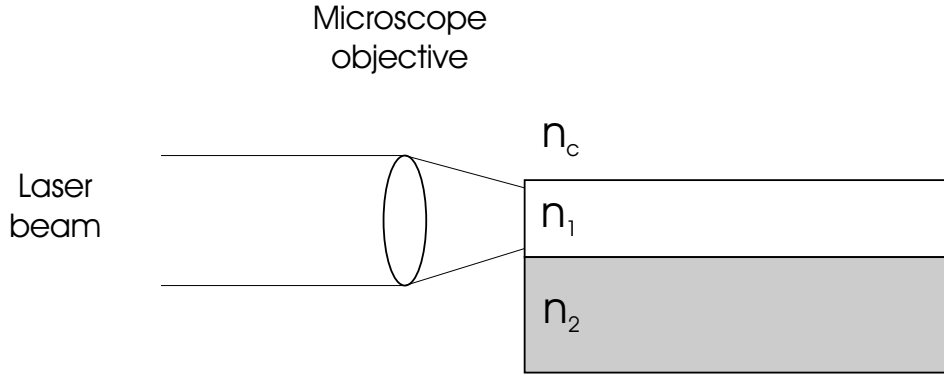


Figure 3.2: End-fire coupling.

3.2.2 Prism couplers

The coupling of the light into a waveguide with a prism coupling is described in section 4.3.

3.2.3 Grating couplers

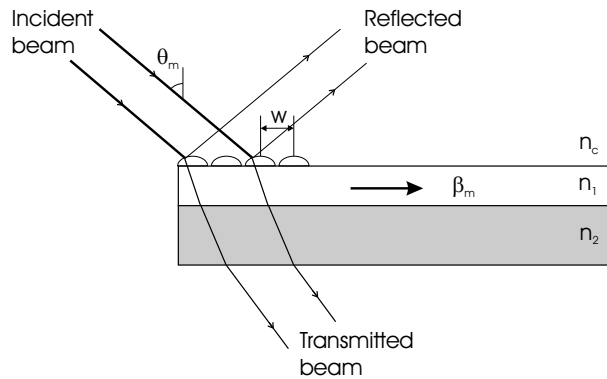


Figure 3.3: Grating coupler.

Like the prism coupler, the grating coupler allows the phase matching between a particular waveguide mode and an unguided optical beam which is incident at an oblique angle to the surface of the waveguide, as shown in Fig. 3.3.

In a grating coupler the waveguide is covered by a dielectric grating which leads to a distributed coupling between a waveguide mode and a laser beam [18]. In the region underneath the grating, the waveguide modes are per-

turbed and they have a set of spatial harmonics, and the propagation constant in the waveguide direction is given by:

$$\beta_\nu = \beta_m + \frac{2\pi\nu}{w}, \quad (3.2)$$

where $\nu = 0, \pm 1, \pm 2, \dots$, w is the periodicity of the grating and β_m is the propagation constant of a particular mode in the waveguide region not covered by the grating. The phase matching condition is given by:

$$\beta_\nu = k_0 n_c \sin \theta_m. \quad (3.3)$$

The grating coupler can be used to selectively transfer energy from an optical beam to a particular waveguide mode by properly choosing the angle of incidence θ_m .

The grating can be used as an output coupler as well, energy from waveguide modes will be coupled out at a specific angle θ_m corresponding to a particular mode [17].

3.3 Jones matrix formulation

The Jones calculus, invented in 1940 by R.C Jones, is a powerful 2×2 matrix method in which the state of polarization is represented by a two-component vector, while each optical element is represented by a 2×2 matrix. The overall matrix for the whole system is obtained by multiplying all the matrices, and the polarization state of the transmitted light is computed by multiplying the vector representing the input beam by the overall matrix.

A monochromatic plane wave of frequency ν traveling in z direction is completely characterized by the Jones vector:

$$\mathbf{J} = \begin{pmatrix} J_x \\ J_y \end{pmatrix} = \begin{pmatrix} E_{0x}e^{i\delta x} \\ E_{0y}e^{i\delta y} \end{pmatrix} \quad (3.4)$$

The Jones vectors for several special polarization states are provided in Table 3.1.

The light propagation in a birefringent crystal consists of a linear superposition of two eigenwaves, which have well-defined phase velocities and directions of polarization. In a uniaxial crystal, these eigenwaves are the ordinary and the extraordinary wave. The directions of polarization for these eigenwaves are mutually orthogonal and are called the "slow" and "fast" axes of the crystal for that direction of propagation.

Retardation plates are usually cut in such a way that the c axis lies in the plane of the plates surfaces. Thus the propagation direction of normally

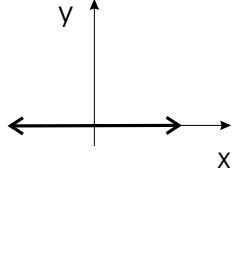
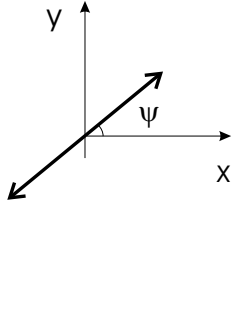
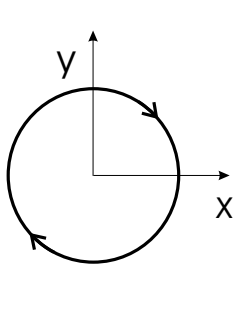
Linearly polarized wave in x direction	$\begin{pmatrix} 1 \\ 0 \end{pmatrix}$	
Linearly polarized, plane of polarization making angle ψ with x axis	$\begin{pmatrix} \cos \psi \\ \sin \psi \end{pmatrix}$	
Right circularly polarized	$\frac{1}{\sqrt{2}} \begin{pmatrix} 1 \\ i \end{pmatrix}$	

Table 3.1: Jones vectors.

incident light is perpendicular to the c axis. In formulating the Jones matrix method, one assume that there is no reflection of light from either surface of the plate and the light is totally transmitted trough the plate surfaces.

Figure 3.4 shows a retardation plate. The x and z axes are fixed laboratory axes. The "fast" and "slow" axes of the crystal (e.g. the extraordinary and the ordinary axes of a negative uniaxial crystal) make an angle φ with the fixed x and z laboratory axes, called the azimuth angle.

The Jones matrix of a retardation plate is given by:

$$W_0 = \begin{pmatrix} e^{-in_s 2\pi l/\lambda} & 0 \\ 0 & e^{-in_f 2\pi l/\lambda} \end{pmatrix}, \quad (3.5)$$

where l is the thickness of the plate, λ is the vacuum wavelength of the light beam, n_s and n_s are the "slow" and "fast" refractive indices.

This matrix can be rewritten in the form:

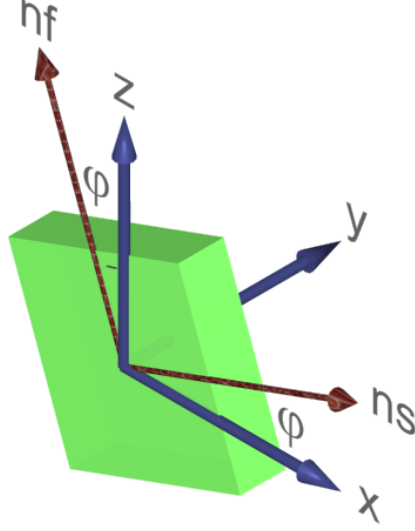


Figure 3.4: Retardation plate.

$$W_0 = e^{-i\phi} \begin{pmatrix} e^{-i\Gamma/2} & 0 \\ 0 & e^{i\Gamma/2} \end{pmatrix}, \quad (3.6)$$

where $\Gamma = (n_s - n_f) \frac{2\pi l}{\lambda}$ is the phase retardation and $\phi = \frac{1}{2}(n_s + n_f) \frac{2\pi l}{\lambda}$ is the mean absolute phase change.

Γ is a measure of the relative change in phase, while ϕ is an absolute phase change.

If one considers an incident light beam with an arbitrary polarization state described by the Jones vector $V = \begin{pmatrix} V_x \\ V_z \end{pmatrix}$, one can write the transformation due to the retardation plate as:

$$\begin{pmatrix} V'_x \\ V'_z \end{pmatrix} = R(-\phi) W_0 R(\phi) \begin{pmatrix} V_x \\ V_z \end{pmatrix}, \quad (3.7)$$

where W_0 is given by eq. 3.6 and $R(\phi)$ is the rotation matrix given by:

$$R(\phi) = \begin{pmatrix} \cos\phi & \sin\phi \\ -\sin\phi & \cos\phi \end{pmatrix}. \quad (3.8)$$

Thus, a retardation plate is characterized by its phase retardation Γ and its azimuth angle ϕ , and is represented by the product of three matrices:

$$W = R(-\phi) W_0 R(\phi) \quad (3.9)$$

The Jones matrix of a retardation plate is a unitary matrix, with the property $W^*W = 1$, where W^* is the Hermitian conjugate of W .

3.4 Electro-optic effect of BaTiO₃

The propagation of optical radiation in a crystal can be described completely in terms of the impermeability tensor η_{ij} , defined by $\boldsymbol{\eta} = \epsilon_0 \boldsymbol{\epsilon}^{-1}$ [19]. The index ellipsoid representation is a good method for finding the two directions of polarization and the corresponding refractive indices. The general form of the index ellipsoid is given by:

$$\sum \eta_{ij} x_i x_j = 1, \quad i, j = 1, 2, 3 \quad (3.10)$$

The index ellipsoid takes the simplest form in the principal coordinate system:

$$\frac{x^2}{n_x^2} + \frac{y^2}{n_y^2} + \frac{z^2}{n_z^2} = 1, \quad (3.11)$$

where x , y and z are the principal axes of the index ellipsoid, for which the \mathbf{D} and \mathbf{E} vectors are parallel. $\frac{1}{n_x^2}$, $\frac{1}{n_y^2}$ and $\frac{1}{n_z^2}$ are the principal values of the impermeability tensor η_{ij} .

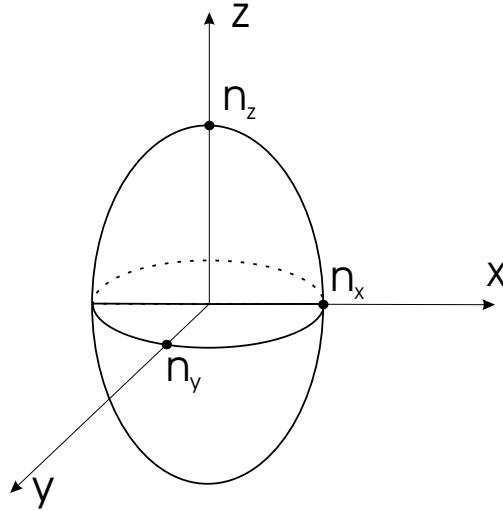


Figure 3.5: The index ellipsoid. The coordinates (xyz) are the principal axes and (n_x, n_y, n_z) are the principal refractive indices of the crystal.

The electro-optic effect results in changes of the refractive index (changes in the optical dielectric impermeability tensor) by an applied electric field.

According to the quantum theory of solids, the impermeability tensor depends on the distribution of the charge in crystal. The application of an electric field results in a redistribution of the bond charges and possibly a slight deformation of the ion lattice. The net result is a change in the optical impermeability tensor. The electro-optic coefficients are defined as:

$$\eta_{ij}(\mathbf{E}) = \eta_{ij}^0 + r_{ijk}E_k + s_{ijkl}E_kE_l + \dots, \quad (3.12)$$

where \mathbf{E} is the applied electric field, r_{ijk} are the linear (or Pockels) electro-optic coefficients and s_{ijkl} are the quadratic (or Kerr) electro-optic coefficients. For crystals with non-centrosymmetric point groups, the linear electro-optic effect (Pockels effect) is dominant. For the centrosymmetric crystals, the linear electro-optic effect vanishes and the quadratic effect (Kerr effect) becomes dominant. The index ellipsoid equation in the presence of an applied electric field is given by:

$$\eta_{ij}(\mathbf{E})x_ix_j = 1 \quad (3.13)$$

η_{ij} is a symmetric tensor and one can write the following permutation symmetries:

$$r_{ijk} = r_{jik} \quad (3.14)$$

$$s_{ijkl} = s_{jikl} \quad (3.15)$$

$$s_{ijkl} = s_{ijlk} \quad (3.16)$$

Because of the permutation symmetries it is convenient to use the contracted indices defined as: $11 \rightarrow 1, 22 \rightarrow 2, 33 \rightarrow 3, 23, 32 \rightarrow 4, 13, 31 \rightarrow 5, 12, 21 \rightarrow 6$. The electro-optic tensor of BaTiO₃ in contracted notation is given by the 3 x 6 matrix:

$$\begin{pmatrix} 0 & 0 & r_{13} \\ 0 & 0 & r_{13} \\ 0 & 0 & r_{33} \\ 0 & r_{51} & 0 \\ r_{51} & 0 & 0 \\ 0 & 0 & 0 \end{pmatrix} \quad (3.17)$$

The linear electro-optic effect of tetragonal BaTiO₃

The impermeability tensor of BaTiO₃ $\boldsymbol{\eta} = \epsilon_o \boldsymbol{\epsilon}^{-1}$ is a 3 x 3 matrix:

$$\boldsymbol{\eta} = \begin{pmatrix} \eta_{11} & \eta_{12} & \eta_{13} \\ \eta_{21} & \eta_{22} & \eta_{23} \\ \eta_{31} & \eta_{32} & \eta_{33} \end{pmatrix} = \begin{pmatrix} \eta_1 & \eta_6 & \eta_5 \\ \eta_6 & \eta_2 & \eta_4 \\ \eta_5 & \eta_4 & \eta_3 \end{pmatrix} \quad (3.18)$$

The matrix from the right side is written in contracted notation. The linear electro-optic effect can be expressed by the vectorial relation:

$$\eta_{ij}(\mathbf{E}) = \eta_{ij}^0 + r_{ijk}^s E_k + p_{ijkl}^{\mathbf{E}} s_{kl}, \quad (3.19)$$

where r_{ijk}^s is the strain free (clamped) electro-optic coefficient, $p_{ijkl}^{\mathbf{E}}$ is the elasto-optic coefficient at constant electric field and s_{kl} the strain tensor. Taking into account the linear electro-optic effect (Pockels effect) and neglecting the elasto-optic effect, the impermeability tensor of BaTiO₃ in the presence of an external electric field takes the form:

$$\eta = \begin{pmatrix} \eta_o + r_{13}E_z & 0 & r_{51}E_x \\ 0 & \eta_o + r_{13}E_z & r_{51}E_y \\ r_{51}E_x & r_{51}E_y & \eta_e + r_{33}E_z \end{pmatrix} \quad (3.20)$$

3.5 Mach-Zehnder modulators with the applied electrical field perpendicular to the optical axis

For a c-axis BTO thin-film, the optical axis is perpendicular to the plane of the film. With the electrodes deposited besides the waveguide, the applied electrical field is perpendicular to the optical axis as is shown in Fig. 3.6.

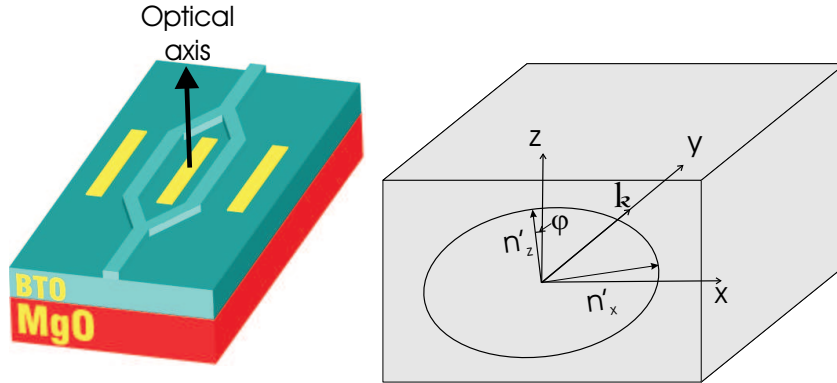


Figure 3.6: c-axis film Mach-Zehnder modulator.

Taking into account the linear electro-optic effect (Pockels effect) produced by an applied electric field along x axis ($E_x \neq 0, E_y = 0, E_z = 0$) and neglecting the elasto-optic effect, the impermeability tensor of the BTO crystal given

by eq. 3.20 is

$$\boldsymbol{\eta}_{BTO} = \begin{pmatrix} \eta_o & 0 & r_{51}E_x \\ 0 & \eta_o & 0 \\ r_{51}E_x & 0 & \eta_e \end{pmatrix}, \quad (3.21)$$

with $\eta_o = \frac{1}{n_o^2}$, $\eta_e = \frac{1}{n_e^2}$, n_o and n_e being the ordinary and the extraordinary refractive index.

Using the relation 3.10, the equation of the index ellipsoid is given by:

$$\frac{x^2}{n_o^2} + \frac{y^2}{n_o^2} + \frac{z^2}{n_e^2} + 2r_{51}E_x xz = 1 \quad (3.22)$$

In the principal coordinate system (x' , y' , z') the equation of the index ellipsoid takes the simplest form and the impermeability tensor becomes diagonal. This corresponds to a coordinate transformation by a rotation of angle φ around the y axis. The angle of rotation depends on the external applied electric field E_x and is given by:

$$\varphi = \arctan \left[\frac{1}{2r_{51}E_x} \left(\frac{1}{n_e^2} - \frac{1}{n_o^2} - \sqrt{\left(\frac{1}{n_o^2} - \frac{1}{n_e^2} \right) + 4r_{51}^2 E_x^2} \right) \right] \quad (3.23)$$

The impermeability tensor in the principal coordinate system becomes

$$\boldsymbol{\eta}'_{BTO} = \begin{pmatrix} \eta_o + r_{51}E_x \tan \varphi & 0 & 0 \\ 0 & \eta_o & 0 \\ 0 & 0 & \eta_e - r_{51}E_x \tan \varphi \end{pmatrix}, \quad (3.24)$$

and the the equation of the index ellipsoid takes the form:

$$\left(\frac{1}{n_o^2} + r_{51}E_x \tan \varphi \right) x'^2 + \frac{y'^2}{n_o^2} + \left(\frac{1}{n_e^2} - r_{51}E_x \tan \varphi \right) z'^2 = 1 \quad (3.25)$$

Using the approximation $\Delta n_i \simeq -\frac{n^3}{2} \Delta \eta_{ii}$ which is valid for small variations of the refractive index due to the external applied electric field, one can write the new refractive indices in the principal coordinate system:

$$n'_x = n_o - \frac{n_o^3}{2} r_{51} E_x \tan \varphi, \quad (3.26)$$

$$n'_y = n_o, \quad (3.27)$$

$$n'_z = n_e + \frac{n_e^3}{2} r_{51} E_x \tan \varphi \quad (3.28)$$

We can treat the Mach-Zehnder modulators arms as retardation plates, making use of Jones formalism described in chapter 3.2.3. Thus, the Jones vector

at the input of the device is described by $V_0 = \begin{pmatrix} \cos \psi \\ \sin \psi \end{pmatrix}$, assuming that the incoming light is linear polarized and the polarization direction makes an angle ψ with the plane of the sample. For in-plane polarized light (TE polarization), Jones input vector is $\begin{pmatrix} 1 \\ 0 \end{pmatrix}$. Using eq. 3.9 and eq. 3.6, the Jones matrix of the first arm of the Mach-Zehner modulator which is under the influence of the external electric field is given by

$$W_1 = R(-\varphi) e^{-i\phi_1} \begin{pmatrix} e^{-i\Gamma_1/2} & 0 \\ 0 & e^{i\Gamma_1/2} \end{pmatrix} R(\varphi) \quad (3.29)$$

where $R(-\varphi)$ and $R(\varphi)$ are rotation matrices of angle φ given by eq. 3.23, $\Gamma_1 = (n'_x - n'_z) \frac{2\pi l}{\lambda}$ is the phase retardation and $\phi_1 = \frac{1}{2}(n'_x + n'_z) \frac{2\pi l}{\lambda}$ is the mean absolute phase change for this arm. Using eq. 3.23 and eq. 3.28 we find:

$$\begin{aligned} \Gamma_1 &= \frac{2\pi l}{\lambda} \times \\ &\times \left[n_o - n_e - \frac{1}{4} (n_o^3 + n_e^3) \left(\frac{1}{n_e^2} - \frac{1}{n_o^2} - \sqrt{\left(\frac{1}{n_o^2} - \frac{1}{n_e^2} \right) + 4r_{51}^2 E_x^2} \right) \right] \quad (3.30) \\ \phi_1 &= \frac{1}{2} \left(n_o + n_e - \frac{1}{2} r_{51} E_x \tan \varphi (n_o^3 - n_e^3) \frac{2\pi l}{\lambda} \right) \quad (3.31) \end{aligned}$$

For the second arm, the phase retardation and the the mean phase change are:

$$\Gamma_2 = \frac{2\pi l}{\lambda} (n'_x - n'_z) = \frac{2\pi l}{\lambda} (n_o - n_e) \quad (3.32)$$

$$\phi_2 = \frac{1}{2} (n_o + n_e) \frac{2\pi l}{\lambda} \quad (3.33)$$

The Jones matrix of the second arm is:

$$W_2 = e^{-i\phi_2} \begin{pmatrix} e^{-i\Gamma_2/2} & 0 \\ 0 & e^{i\Gamma_2/2} \end{pmatrix} \quad (3.34)$$

The Jones vectors after propagation through the modulator arms are given by:

$$V_1 = W_1 V_0 \frac{1}{2} \quad (3.35)$$

$$V_2 = W_2 V_0 \frac{1}{2} \quad (3.36)$$

After the interference of the two beams, the output Jones vector is $V = V_1 + V_2 = \begin{pmatrix} A_{TE} \\ A_{TM} \end{pmatrix}$. The output intensity is $I = |A_{TE}|^2 + |A_{TM}|^2$. Fig. 3.7 shows the transmitted intensity of a Mach-Zehnder modulator as a function of the electric field applied perpendicular to the optical axis (thick line). The incoming light has in-plane polarization (TE polarized light).

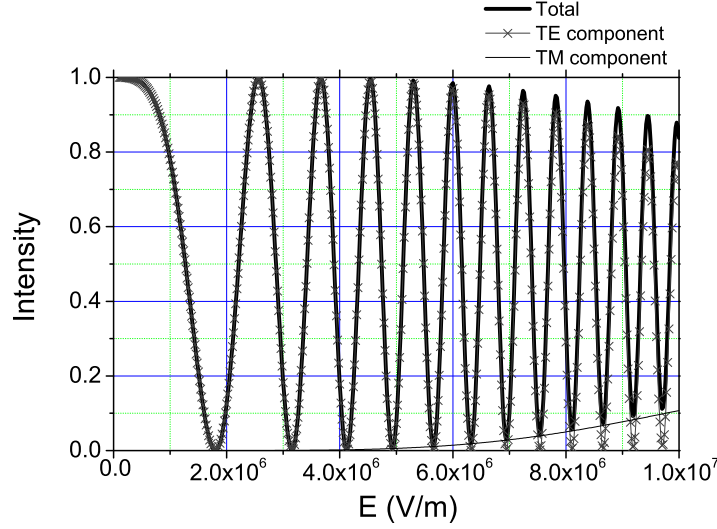


Figure 3.7: Output intensity of a Mach-Zehnder modulator with driving field perpendicular to the optical axis. Numerical values used for simulation: $n_o = 2.351$, $n_e = 2.330$, $r_{51} = 80$ pm/V, $\lambda = 1550$ nm, $\psi = 0$ degrees.

On the same plot there are the TE component (crosses + line) and TM component (thin line). For the normal operation regime at low applied electric field the device is polarization maintaining. After increasing of the applied field (> 5 V/ μ m), the TM component starts to build up, as it can be seen from Fig. 3.7.

From eq. 3.30 and eq. 3.23 it results that the phase shift induced by the external electric field is a quadratic function of the field magnitude [20]. As a consequence, by applying simultaneously opposite electric fields on both arms of the modulator $E(t)$, $-E(t)$ (so called "push-pull" geometry), the output light intensity will remain unchanged. Figure 3.8 illustrates this situation.

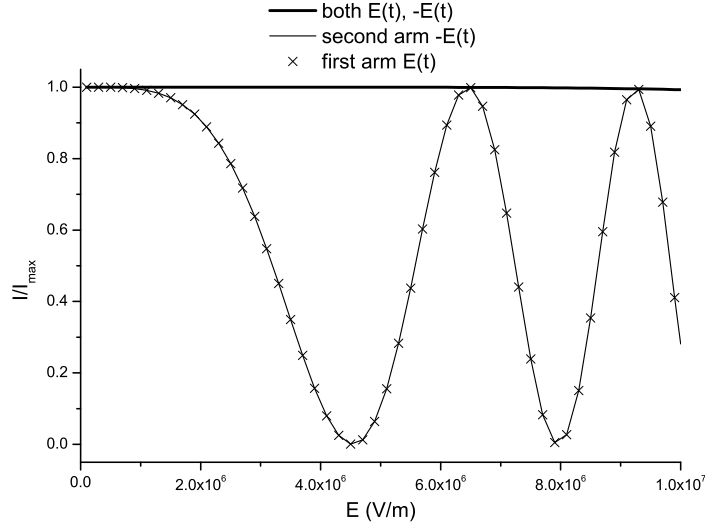


Figure 3.8: Calculated response for "push-pull" geometry, applied field perpendicular to optical axis.

3.6 Mach-Zehnder modulators with the applied electrical field parallel to the optical axis

For the a-axis oriented films Mach-Zehnder modulators the electric field is applied in the direction of the optical axis and the impermeability tensor in the presence of the electric field has a diagonal form:

$$\eta_{BTO} = \begin{pmatrix} \eta_o + r_{13}E_z & 0 & 0 \\ 0 & \eta_o + r_{13}E_z & 0 \\ 0 & 0 & \eta_e + r_{33}E_z \end{pmatrix}, \quad (3.37)$$

r_{13} and r_{33} being the Pockels coefficients and E_z the applied electrical field ($E_x = E_y = 0$).

The index ellipsoid is given by the equation:

$$\left(\frac{1}{n_o^2} + r_{13}E_z\right)x^2 + \left(\frac{1}{n_o^2} + r_{13}E_z\right)y^2 + \left(\frac{1}{n_o^2} + r_{33}E_z\right)z^2 = 1 \quad (3.38)$$

As it can be seen, in this case the impermeability tensor has a diagonal form, and therefore the laboratory coordinate system coincides with principal axes of the index ellipsoid.

By applying a driving electric field to one arm of the optical modulator, the refractive indices changes. Using the approximation $\Delta n_i \simeq -\frac{n^3}{2}\Delta\eta_{ii}$ ($i = 1, 2, 3$) for small variations of the refractive index due to the external applied electric field and the impermeability tensor (eq. 3.37), the new refractive indices in the presence of the external electrical field are:

$$n'_x = n'_y = n_o - \frac{n_o^3}{2}r_{13}E_z; \quad n'_z = n_e - \frac{n_e^3}{2}r_{33}E_z \quad (3.39)$$

The Jones matrices of the modulator arms are, according with 3.5 :

$$W_1 = \begin{pmatrix} e^{-i\left(n_e - \frac{n_e^3}{2}r_{33}E_z\right)\frac{2\pi l}{\lambda}} & 0 \\ 0 & e^{-i\left(n_o - \frac{n_o^3}{2}r_{13}E_z\right)\frac{2\pi l}{\lambda}} \end{pmatrix} \quad (3.40)$$

$$W_2 = \begin{pmatrix} e^{-in_e 2\pi l/\lambda} & 0 \\ 0 & e^{-in_o 2\pi l/\lambda} \end{pmatrix}, \quad (3.41)$$

The Jones vectors after propagation through the modulator arms are given by

$$V_1 = W_1 V_0 \frac{1}{2} \quad (3.42)$$

$$V_2 = W_2 V_0 \frac{1}{2}, \quad (3.43)$$

where $V_0 = \begin{pmatrix} \cos \psi \\ \sin \psi \end{pmatrix}$ is the input Jones vector, ψ being the angle between the polarization direction of the incoming light and the plane of the sample. After the interference of the two beams, the output Jones vector is $V = V_1 + V_2 = \begin{pmatrix} A_{TE} \\ A_{TM} \end{pmatrix}$. The output intensity is

$$I = |A_{TE}|^2 + |A_{TM}|^2 = \frac{1}{4} \left| e^{i\frac{2\pi l}{\lambda}\left(n_e - \frac{n_e^3}{2}r_{33}^{eff}E_z\right)} + e^{-i\frac{2\pi l}{\lambda}n_e} \right|^2 \quad (3.44)$$

Applying the trigonometric formula $\cos \alpha \cos \beta + \sin \alpha \sin \beta = \cos(\alpha - \beta)$, one can write the transmitted intensity as

$$I = \frac{1}{2} \left[1 + \cos \left(\frac{2\pi l}{\lambda} \frac{n_e^3}{2} r_{33}^{eff} E_z \right) \right] \quad (3.45)$$

Assuming that the electric field E_z can be expressed as $E_z = \frac{U}{d}$, where U is the voltage applied to the electrodes and d the electrodes spacing, one

can deduce the half wave voltage V_π necessary to switch the light from the maximum intensity to zero

$$V_\pi = \lambda \frac{d}{l} \frac{1}{n_e^3 r_{33}^{eff}} \quad (3.46)$$

If the half wave voltage V_π is known from the experimental data, the effective electro-optic coefficient r_{33}^{eff} can be determined with:

$$r_{33}^{eff} = \frac{\lambda d}{V_\pi l n_e^3} \quad (3.47)$$

Figure 3.9 shows the transmitted intensity of a Mach-Zehnder modulator as a function of the electric field applied parallel to the optical axis. The incoming light has in-plane polarization (TE polarized light).

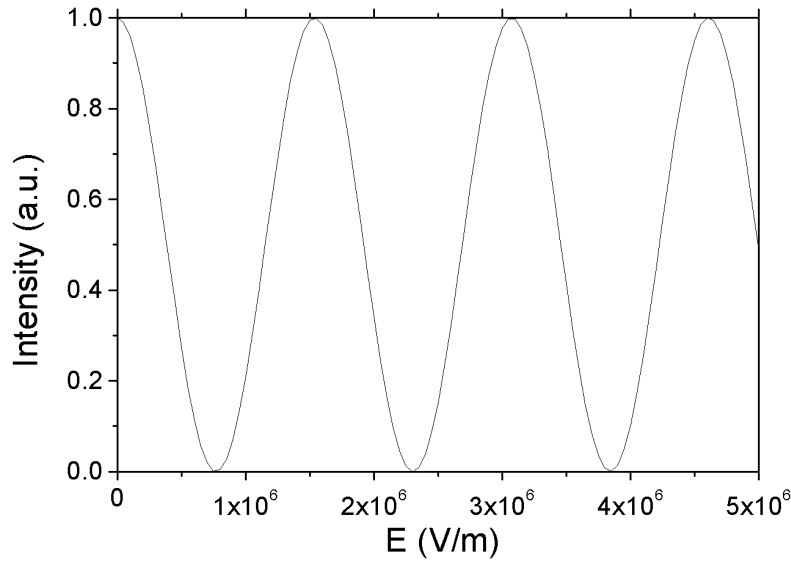


Figure 3.9: Output intensity of a Mach-Zehnder modulator with driving field along the optical axis. Numerical values used for simulation: $n_o = 2.365$, $n_e = 2.353$, $r_{33}^{eff} = 50$ pm/V, $\lambda = 1550$ nm.

Chapter 4

Experimental

4.1 Experimental techniques

4.1.1 Pulsed laser deposition

Pulsed laser deposition is a physical vapor deposition technique for growing high quality films. This technique offers the advantage of stoichiometric transfer of material from the target to the deposited film and a high deposition rate, up to 1 nm/s. Figure 4.1 shows a sketch of the PLD-system. A short pulsed laser beam from an excimer laser is focused onto a cylindrical rotating target. The pulse energy of typically 1 J/pulse leads to the immediate formation of a plasma due to the high energy density of 3-5 J/cm² at the target surface. The plasma contains energetic neutral atoms, ions and molecules and reaches the substrate surface with a broad energy distribution of 0.1 to > 10 eV [21]. This technique has been successfully used to grow numerous perovskites exhibiting superconducting [22, 23], ferroelectric [24] or electro-optic properties [25].

4.1.2 X-ray diffraction

X-ray diffraction is a widely used method to investigate the structural properties of crystals, polycrystalline and amorphous samples or layer systems. It provides information on the crystal structure, orientation and quality of the single crystals, grain size (polycrystalline materials), layer thickness, surface roughness [26]. The X-ray measurements within this work were performed with a *Philips X'pert MRD* four-circle diffractometer with a copper x-ray tube (characteristic wavelength Cu-K α_1 , $\lambda = 1.54056 \text{ \AA}$). Fig. 4.2 shows a sketch of the four-circle geometry.

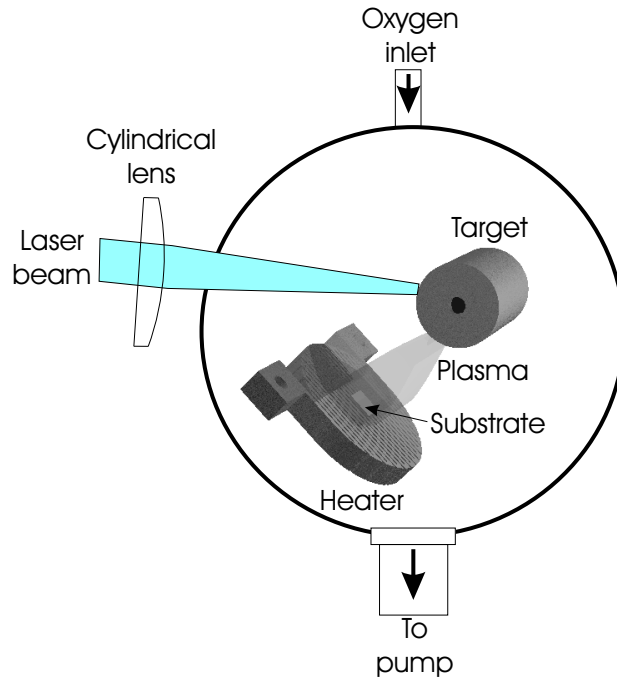


Figure 4.1: Sketch of a PLD-system.

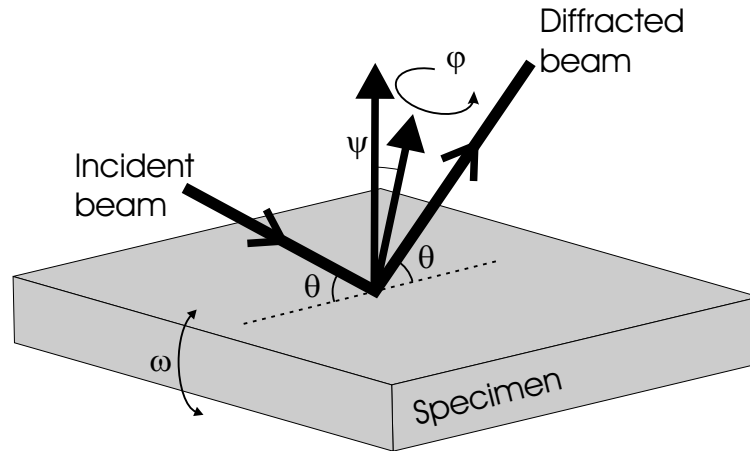


Figure 4.2: Sketch of the four-circle x-ray diffractometry.

The detector angle (2θ) and the sample angle (θ or ω) can be rotated independently in the plane defined by the incident and the refracted beams. This enables measuring the interplanar distances for the planes parallel to the substrate surface. The ϕ and ψ rotations permit the determinations of interplanar distances of the planes that are not parallel with the substrate

plane.

The incident x-ray beam is reflected from parallel planes of atoms in the crystal, with each plane reflecting only a very small fraction of the radiation. The diffracted beams are found when the reflections from parallel planes of atoms interfere constructively (Fig. 4.3) [27]. Constructive interference of radiation from successive planes occurs when the path difference is an integer number n of wavelengths λ (Bragg law) [27]:

$$2d \sin \theta = n\lambda, \quad n = 1, 2, 3, \dots \quad (4.1)$$

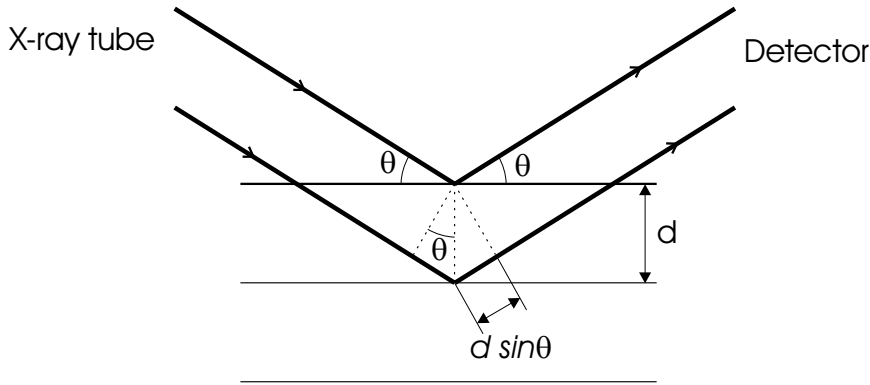


Figure 4.3: X-ray diffraction in symmetrical reflection geometry.

For epitaxial thin film measurements, the in-plane lattice constant can be determined from a normal $\theta - 2\theta$ scan. The lattice parameters are calculated using:

$$\frac{1}{d_{hkl}^2} = \frac{h^2}{a^2} + \frac{k^2}{b^2} + \frac{l^2}{c^2}, \quad (4.2)$$

where a , b , c are the unit cell constants, (hkl) are the Miller indices and d_{hkl} the distance between the (hkl) planes. To measure the in-plane lattice parameter of the tetragonal epitaxial films, the grazing angle geometry may be used. Thus, choosing the angle $\psi \simeq 45^\circ$ the $(h0h)$ reflections can be measured. Also other particular values of the ψ angle are suitable to determine the in-plane lattice parameter (for example (103) reflection).

The crystalline quality of the epitaxial films can be determined by measuring the rocking curve or ω scan of a Bragg reflection. The full width at the half maximum (FWHM) of the rocking curve provides a measure of the spread in the orientation of the atomic layers parallel to the substrate plane.

To study the thin film orientation in the substrate plane, ϕ scans of the substrate and film $(h0h)$ reflections are measured.

Grazing incidence x-ray measurements are used for phase analysis of the polycrystalline thin films [28]. The small incidence angle (usually smaller than 10°) limits the penetration depth, so that a significant part of the diffracted beams will originate from the uppermost part of the sample. However, the well oriented thin films (epitaxial films) might show no reflection if grazing incidence is used.

4.1.3 Rutherford backscattering spectrometry

Rutherford backscattering spectrometry (RBS) is an accurate nondestructive technique for measuring the stoichiometry, layer thickness, quality of the interfaces and crystalline perfection of thin films. RBS offers quantitative determination of absolute concentrations of multi-elemental thin films.

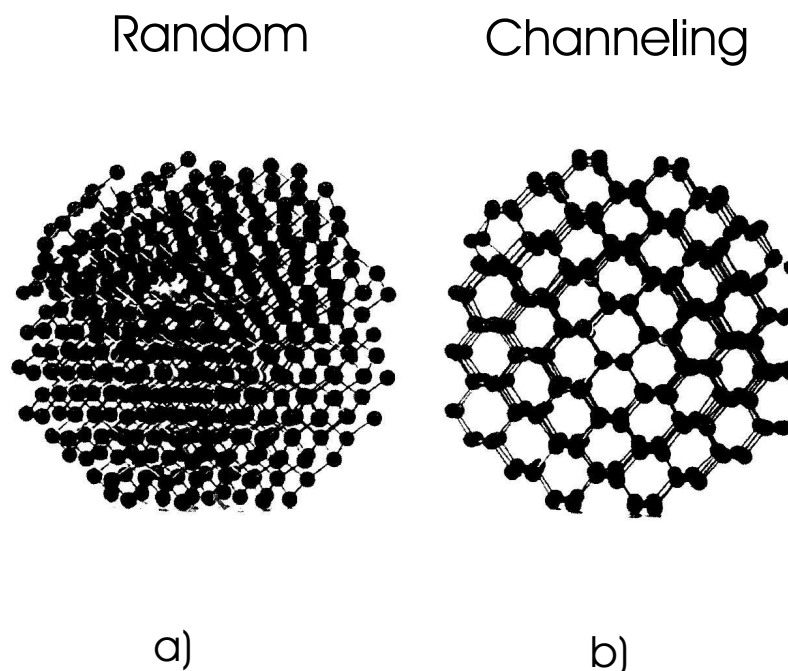


Figure 4.4: Rutherford backscattering. a) Random experiments; b) channeling experiments.

A collimated mono-energetic beam of low mass ions hits the specimen that has to be analyzed. In experiments done for this work we used He^+ ions with an energy of 1.4 MeV. A small fraction of the ions that impinge on the sample are scattered back elastically by the nuclei of the atoms and are collected by a detector. The detector determines the energy of the backscattered ions

resulting in the RBS energy spectrum. The spectra that are obtained give the yield of backscattered particles as a function of their energy. The analysis of the spectra is done off line using modern software (RUMP) [29]. A more detailed description of the technique is given by Ref. [30].

Figure 4.4 shows the two types of RBS experiments for crystalline samples: random and channelling measurements.

In the random experiments, the ion beam is not aligned to the crystallographic directions of the specimen (Fig. 4.4a). The energy distribution of the collected ions provides information about the mass of the sample constituent atoms and the thickness of the layer(s). Information about the interface sharpness between two layers is given by the abruptness of the low energy edge in the random spectrum.

The most common epitaxial films have the same major channelling axis as the substrate. The degree of epitaxy is determined from the ion channelling experiments by a ratio of the elemental signals from the film for channelled and random sample orientations. This ratio is called "minimum yield" χ_{min} and its value provides information about the crystalline perfection of the films. The defects inside the film lead to higher values of the χ_{min} .

4.1.4 Atomic force microscopy

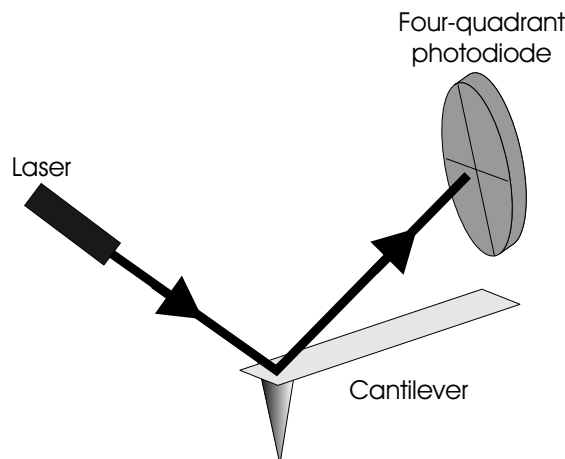


Figure 4.5: Atomic force microscopy: principle of operation.

Atomic force microscopy is one of the most widely used scanning probe microscopy (SPM) technique [31]. The primary purpose of an AFM instrument is to quantitatively measure surface roughness with typically 5 nm lateral and 0.01 nm vertical resolution on all types of samples. The principles on

how the AFM works are illustrated in Fig. 4.5. An atomically sharp tip is scanned over a surface with feedback mechanisms that enable the piezo-electric scanners to maintain the tip at a constant force (to obtain height information), or height (to obtain force information) above the sample surface. Tips are typically made from Si_3N_4 or Si, and extended down from the end of a cantilever. The nanoscope AFM head employs an optical detection system in which the tip is attached to the underside of a reflective cantilever. A diode laser is focused onto the back of a reflective cantilever. As the tip scans the surface of the sample, the laser beam is deflected off the attached cantilever into a four-quadrant photodiode. Feedback from the photodiode difference signal, through software control from the computer, enables the tip to maintain either a constant force or constant height above the sample. In the constant force mode the piezo-electric transducer monitors real time height deviation. In the constant height mode the deflection force on the sample is recorded. The instrument gives a three dimensional topographical maps of the surface of the sample by plotting the local sample height versus horizontal probe tip position.

4.2 Mach-Zehnder Modulators

4.2.1 Device design and fabrication

A waveguide Mach-Zehnder modulator is schematically drawn in Fig. 4.6. It is an interferometrical device in which interference is produced between phase coherent light waves that have travelled over different path length. Light enters to the modulator via a single mode waveguide. A "Y" branch plays the role of the beam splitter and it divides the light into two equal beams that travel through the arms of the modulator which are also single mode waveguides. By applying a voltage to the electrodes, the effective optical path length can be modified via the electro-optic effect. In an ideal modulator of this type, the path lengths and guide characteristics are identical for both arms, so that without applied voltage the split beams recombine in the output waveguide and, as a result of the interference, a maximum intensity is obtained. If an electric field is applied so as to produce a phase change of π radians between the two arms, then the result of interference is a zero optical field at the center of the output waveguide, corresponding to the first order mode. Because the output waveguide is a single mode guide identical to the input guide, the first order mode is cut off, and rapidly dissipates over a short length by substrate radiation.

In order to avoid high losses due to the low in-plane confinement of the

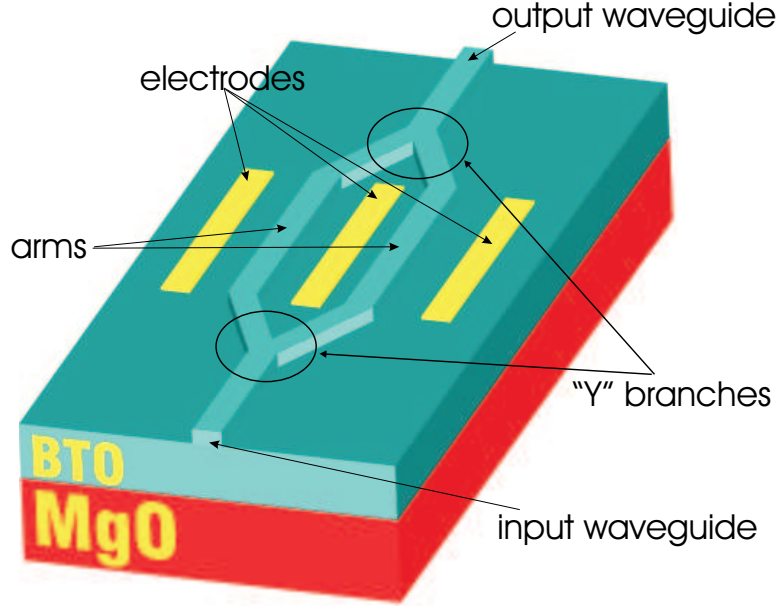


Figure 4.6: Thin film Mach-Zehnder modulator.

light in the strip waveguides, the "fork" angle of the "Y" branches of our modulators has a low value of 1° . Fig. 4.7 shows a microscope photograph of the fork of the thin film Mach-Zehnder modulators. An array of 25 Mach-Zehner modulators are patterned on a 10 x 10 mm sample BaTiO_3 on MgO. The electrodes are 3 mm long and the separation between electrodes is $10\ \mu\text{m}$. Modulators with a smaller electrodes separation of $5\ \mu\text{m}$ have also been prepared. For coupling light into the modulator, flat input and output edges are desirable. Because the MgO substrates are cleavable, good flat edges are obtained by cleaving the modulators, using a method described in the Ph.D. Thesis of Eckau [32]. The result is shown in Fig. 4.8. Around 1 mm of material is removed from each side, resulting in devices of about 8 mm long.

4.2.2 Ridge waveguides

A ridge or rib waveguide is sketched in Figure 4.9. The presence of the ridge on top of the waveguiding layer makes the refractive index in the region beneath it, n'_{eff1} larger than the effective index n_{eff1} in the adjacent regions. Thus, this type of waveguide is equivalent to a rectangular dielectric waveguide and it has been analyzed by Kogelnik [33]. By applying the effective index method he showed that propagation is characterized by a phase

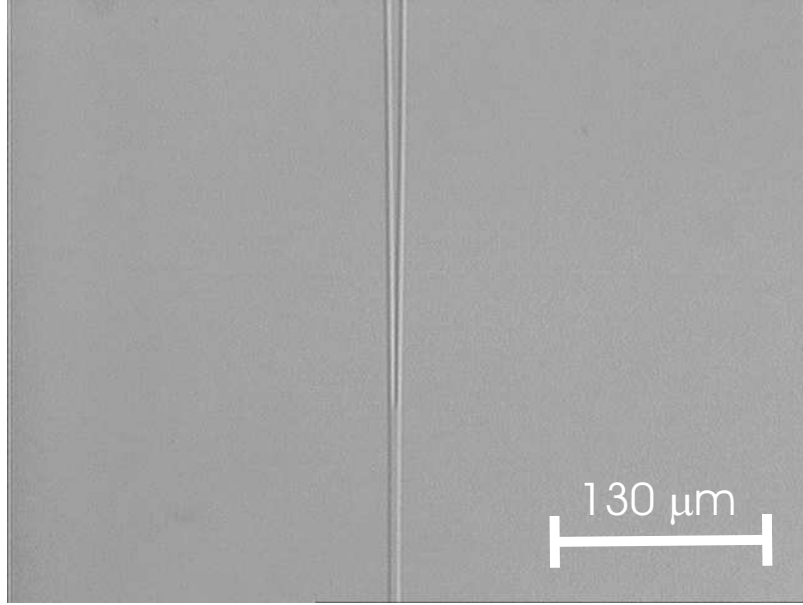


Figure 4.7: Microscope photograph of the "Y" branch, with a fork angle of 1° .

constant $\beta = kN$, where N is given by

$$N^2 = n_{eff1}^2 + b(n_{eff1}^2 - n_2^2) \quad (4.3)$$

where n_{eff1}' is the effective index in a guide having a height equal to the sum of the thickness of the waveguiding layer and the loading strip. The parameter b is a normalized guide index given by $b = (N^2 - n_2^2)/(n_1^2 - n_2^2)$. It is expected that ridge waveguides should have less optical loss than rectangular channel dielectric waveguides, because scattering due to side wall roughness is reduced. On the other hand, the small effective index difference in the lateral direction will be insufficient to limit radiation loss occurring from bends in the guide. Therefore ridge waveguides are suited for straight waveguides and waveguides with small bends and large radii.

With a simulation program based on finite differences written by M. Siegert [34] we calculated the intensity profile of the allowed modes propagating through the ridge waveguides with a specified geometry. The input parameters are the thickness of the BaTiO₃ films, the width and the height of the rib, the refractive indices of the film and substrate and the vacuum wavelength of the light. Thus, we found the geometrical parameters for fabricating single mode ridge waveguides, an important condition for Mach-Zehnder waveguide modulators. A ridge waveguide fabricated on a 1 μm thick BaTiO₃ film deposited on MgO is monomode for a rib width of 2 μm and a rib

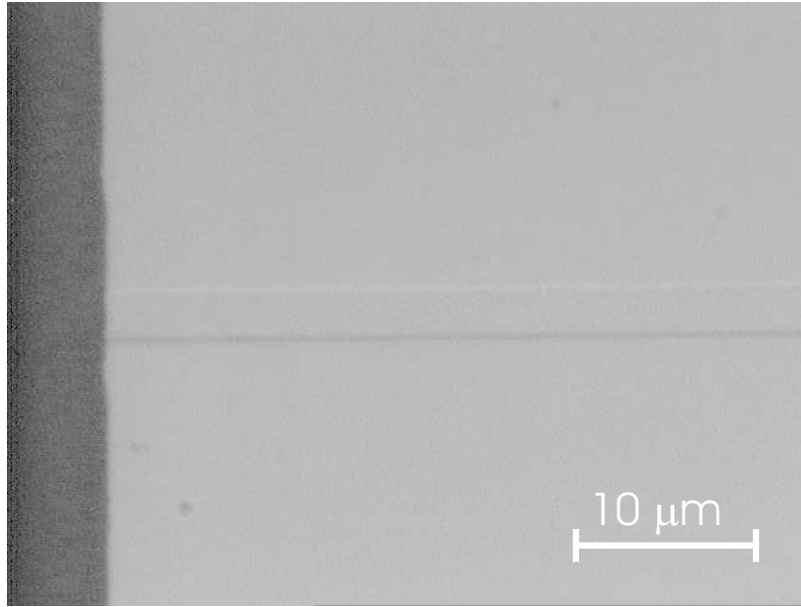


Figure 4.8: Microscope photograph of the cleaved edge of the modulator.

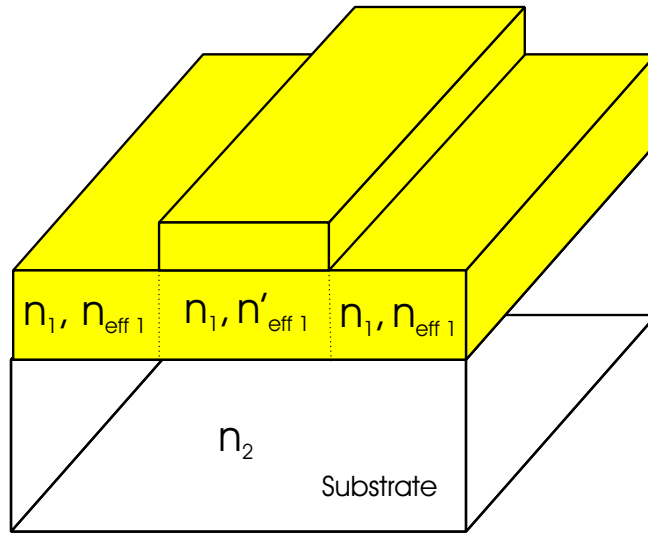


Figure 4.9: Dielectric ridge waveguide. Effective index of refraction, as well as the bulk index, are indicated in the wave-guiding layer. $n'_{eff1} > n_{eff1}$

height of 50 nm at 633 nm wavelength. At 1550 nm wavelength, the rib width can be increased to 3 μm and the rib height to 70 nm. Figure 4.10 shows the simulated intensity profile for TEM_0 mode propagating through a ridge waveguide with the rib width of 3 μm and a rib height of 70 nm at

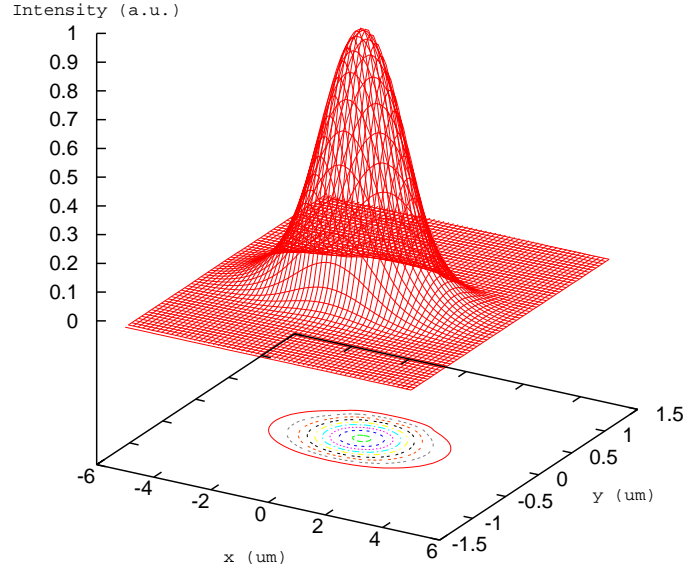


Figure 4.10: Simulated intensity profile of the TEM_0 mode. Ridge width is $3\ \mu\text{m}$, ridge height is $70\ \text{nm}$.

$1550\ \text{nm}$ wavelength. The refractive indices used for this simulation were $n_{\text{BTO}} = 2.253$ and $n_{\text{MgO}} = 1.731$.

Our ridge waveguides were fabricated using standard photolithography and ion beam etching (IBE). After the PLD growth, a mask for IBE was made, as it is schematically described in Fig. 4.11.

A thin chromium layer of $50\ \text{nm}$ was deposited on the sample surface by rf sputtering for improving the adhesion of the photoresist to the BaTiO_3 surface. The processes for waveguide fabrication are listed in Table 4.2.2. After preparing the mask, the sample was dry etched using an IBE machine from OXFORD INSTRUMENTS. For a voltage of $500\ \text{V}$ and a current of $88\ \text{mA}$, the etching rate for BaTiO_3 is about $11\ \text{nm/min}$. After getting the desired etching, the sample has been cleaned with n-Hexan to get rid of the vacuum grease and the etching mask has been removed with acetone, propanol and Cr etching solution. The height of the ridge was measured with a DEKTAK surface profile measuring instrument. Subsequently, a new mask for electrode deposition was made and carefully aligned with respect to the waveguides. A $10\ \text{nm}$ Cr layer and a $90\ \text{nm}$ Au layer were deposited by

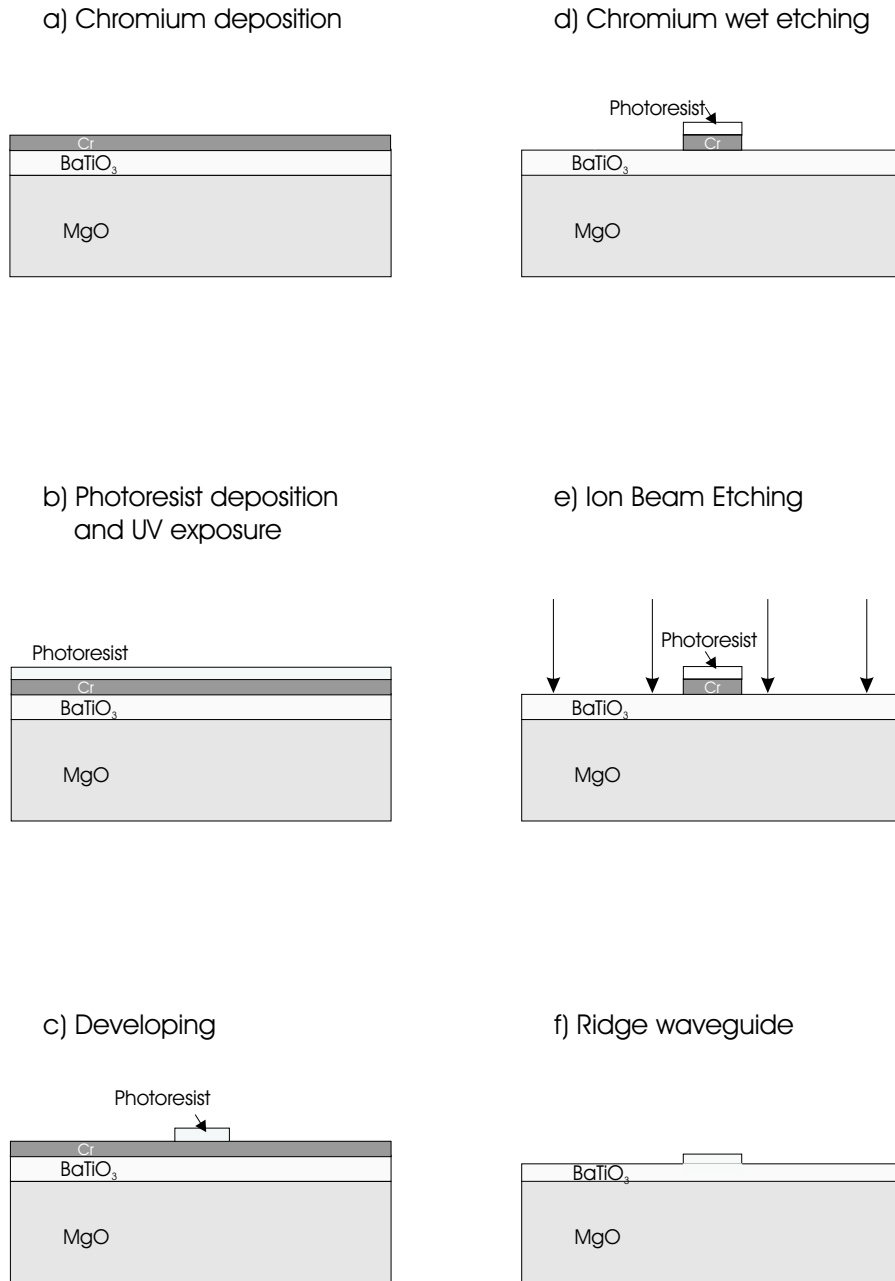


Figure 4.11: Fabrication of the ridge waveguides.

magnetron rf sputtering. The electrodes besides the waveguides were made with a lift-off process. The processes for the electrode fabrication are listed in Table 4.2.

Ridge waveguides fabrication		
Process	Parameters	Comments
cleaning	acetone, propanol	
Cr deposition	50 nm, r.f. sputtering	increasing adhesion of photoresist
adhesive: HMDS (Hexamethyldisilan)	4000 rpm, backed 60 s at 90 °C on hotplate	adhesion increasing
photoresist spinning	photoresist 5206, 6000 rpm, backed 2 min. at 90°C	thickness 0.6 μm
corner removing	15 sec. exposure, 20 sec. developing	
mask exposure	3.6 sec.	
developing	MIF 326:H ₂ O 1:1.125, 30 sec.	
Cr etching	chromium etching solution, cca. 20 sec.	removing Cr besides the mask
ion beam etching	500 V, 88 mA, rotation	etching rate: 11nm/min.
cleaning	n-Hexan, acetone, propanol	vacuum grease and photoresist mask removing
Cr etching	wet etching, cca. 20 sec.	

Table 4.1: Processes and parameters for ridge waveguides fabrication.

4.3 Experimental set-up

Prism coupling setup

A prism coupling setup as described by Ulrich et *al.* [35] has been used for measuring the thickness of the deposited BaTiO₃ films and the in-plane and out-of-plane refractive indices of the films. The method consists of coupling of a laser beam by a prism into a planar dielectric waveguide, which is governed by the angle θ of incidence of the light onto the prism base (Fig. 4.12). This angle θ determines the phase velocity in x direction, $v = c/n_p \sin \theta$ of the incident wave in the prism (index n_p and in the air gap (index n_{air}). Strong coupling of the light into the film occurs only for values of θ for which v equals the phase velocity v_m of the characteristic modes of propagation in the guide ($m = 0, 1, 2, \dots$). Thus, by determining these coupling angles θ_m we

Electrodes fabrication		
Process	Parameters	Comments
adhesive HMDS (Hexamethyldisilan)	4000 rpm, backed 60 s at 90 °C on hotplate	adhesion increasing
photoresist spinning	photoresist 5214, 4000 rpm, backed 5 min. at 90°C	thickness 1.4 μm
corner removing	40 sec. exposure, 30 sec. developing	optical control
mask exposure	5.6 sec.	
developing	MIF 326:H ₂ O 1:1, 30-40 sec.	
Cr, Au deposition	10 nm Cr, 90 nm Au rf sputtering	Cr as adhesion layer
lift-off	lift-off in acetone	checked under microscope

Table 4.2: Processes and parameters for electrodes deposition.

can find experimentally the characteristic propagation constants of the film relative to the propagation constant of the free space:

$$\tilde{N}_m = c/v_m = n_p \sin \theta_m = n_p \sin \left[\epsilon - \arcsin \left(\frac{\sin \alpha_m}{n_p} \right) \right], \quad (4.4)$$

where n_p is the refractive index of the prism, α_m is the angle of incidence of the laser beam to the prism entrance for the mode m and ϵ is the angle of the prism. On the other hand, one can calculate the relative propagation constants N_m from the known dispersion equation of a planar dielectric waveguide, which depends on the refractive index of the film n_1 , refractive indices of the two media adjacent to the film n_2 , n_c (cladding), the thickness of the film d and the polarization of the laser beam, TE or TM. All these parameters are known or can be measured separately. A computer program adjusts the two unknown parameters, the refractive index of the film n_1 and the film thickness d until the calculated theoretical values N_m match as closely as possible the experimental values \tilde{N}_m . The method gives accurate results simply and fast and it has several advantages in comparison with other methods. Only measurements of angles are required, which can be performed conveniently and with high precision. If the film is thick enough to allow the observation of more than two modes of the same polarization, the method becomes self consistent because the two unknown n_1 and d are then

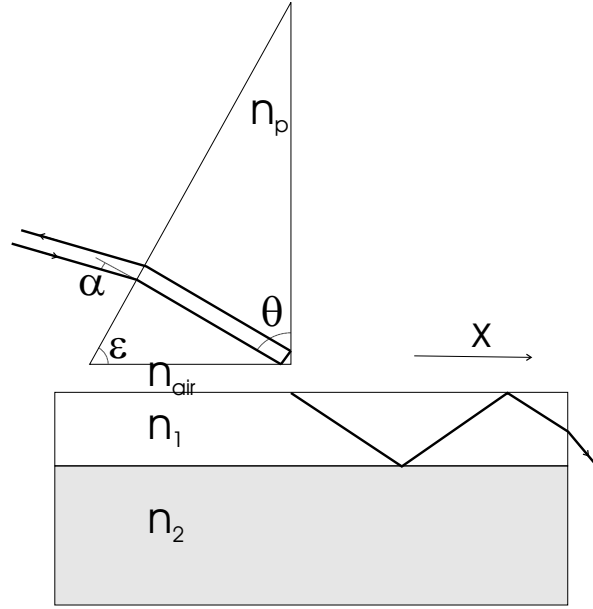


Figure 4.12: Prism coupler.

determined from more than two independent measurements. This improves accuracy and increases the confidence in the results. The method has also some disadvantages: it is not contactless, the film must be thick enough to permit the propagation of at least two modes and strong losses in the film (exceeding 20 - 80 dB/cm) cause a broadening of the modes, that will reduce the accuracy of the measurement.

The prism coupling set-up used in our experiments (see Figure 4.13) has a rutile (TiO_2) prism mounted on a rotating stage driven by a stepper motor. A computer controlled interface controls the angular position of the rotating stage with a precision of 0.001 degrees. The laser beam is supplied by a He-Ne linearly polarized laser at 632.8 nm wavelength. Another He-Ne laser is used for measurements at 1523 nm wavelength, the switching between these two wavelength is accomplished by a detachable mirror M2. The polarization of the two laser beams is 45° .

With the help of a beam polarizer one can select the desired polarization of the light beam in order to measure the in-plane or out-of-plane refractive indices of the film. At the end of the planar waveguide, a bright line detector is mounted on the rotating stage. Scanning the angle α and recording the signal from the bright line detector, a bright line spectrum is recorded. In a similar way, a dark-line spectrum can be recorded with the dark-line detector, and the spectrum has negative peaks corresponding to the angular positions of the coupled modes. For infrared measurements at 1523 nm wave-

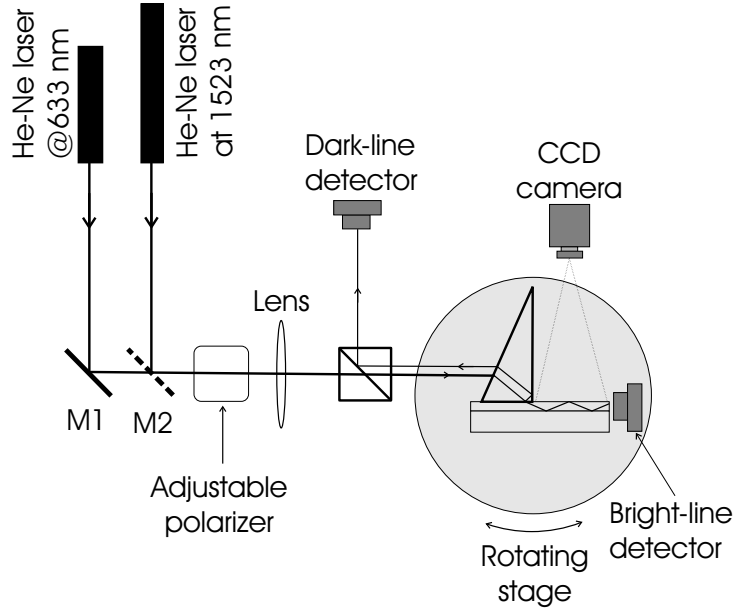


Figure 4.13: Prism coupling set-up for thickness, refractive index and attenuation measurements.

length, the silicon bright-line and dark-line detectors are replaced by InGaAs light detectors. On the same rotating stage, a CCD camera is mounted for recording the image of a mode propagating through the planar waveguide. After processing the image, a plot of the intensity of the scattered light versus distance is obtained. Assuming that the scattering process is uniform along the planar waveguide and the intensity of the scattered light is proportional to the intensity of the light inside the waveguide, one can determine the attenuation coefficient (damping coefficient) of different coupled modes:

$$\ln[I(z) - B] = \ln(I_0) - \alpha_s z, \quad (4.5)$$

where $I(z)$ is the acquired scattering intensity, z is the position in the propagation direction, α_s is the scattering loss coefficient and B is the background light. After extracting the background light, we plot the scattered intensity versus the position z in logarithmic scale and the slope of the curve gives the loss coefficient α_s . The damping coefficient in dB/cm is related to α_s by [17]:

$$D \left[\frac{dB}{cm} \right] = 4.3 \alpha_s [cm^{-1}] \quad (4.6)$$

This method has relatively good accuracy for high loss planar waveguides. If the scattering loss is less than about 1 dB/cm, measurements are difficult

because of the low intensity that must be detected and the accuracy of the method decreases.

Experimental setup for electro-optic measurements

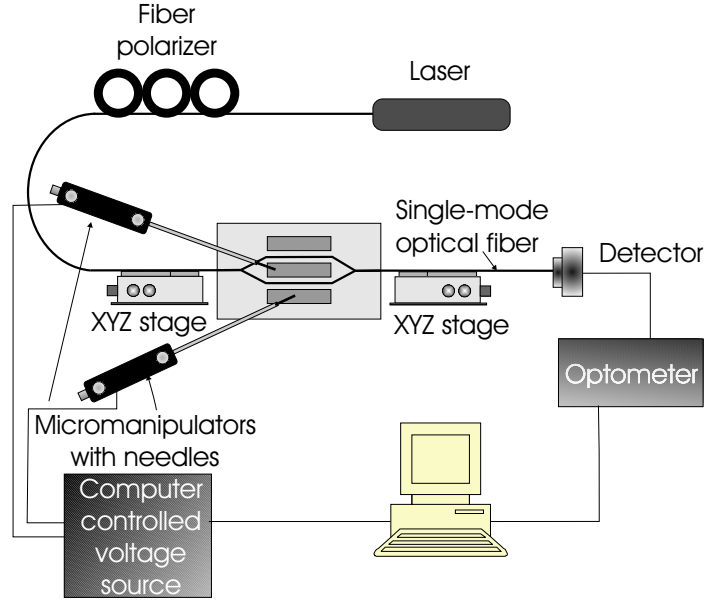


Figure 4.14: Sketch of the experimental setup for electro-optical measurements.

The experimental set-up for the electro-optic measurements is schematically represented in Fig. 4.14. It includes a He-Ne laser for measurement at 633 nm wavelength and a laser diode at 1550 nm wavelength. In both cases the laser beam is coupled into a single mode fiber. A fiber polarizer is inserted for defining the polarization state of the input light (TE or TM). For adjusting the polarization of the incoming beam, an additional a Glan-Thompson cross-polarizer is used together with a microscope objective. The light is end-fire coupled into the waveguide. The output of the waveguide modulator is coupled to another single mode fiber, which leads to a silicon detector. The fibers are aligned to the waveguide with two nano positioning XYZ stages. Contact needles, supported by micromanipulators, are used to apply the voltage to the middle and to one outer electrode. The driving voltage is supplied by a computer controlled dual channel voltage source. The voltage source is able to give an output voltage in the range 0 - 260 V or two independent outputs with a voltage range 0 - 130 V. The signal from the photo detector is processed by a computer controlled optometer. A computer program scans

the driving voltage range (typically 0 V - 100 V) and reads the signal from the detector. A data set is recorded to a file, containing the information for driving voltage and output intensity. Thus, the transmitted optical intensity is measured as a function of the applied voltage. The measuring program permits to set the scanning time from few seconds to tens of minutes. Also, a poling step can be inserted prior to the measurements.

The frequency response of the modulator up to 1 MHz was measured with a modified setup for the electro-optic measurements, as is shown in Fig. 4.15.

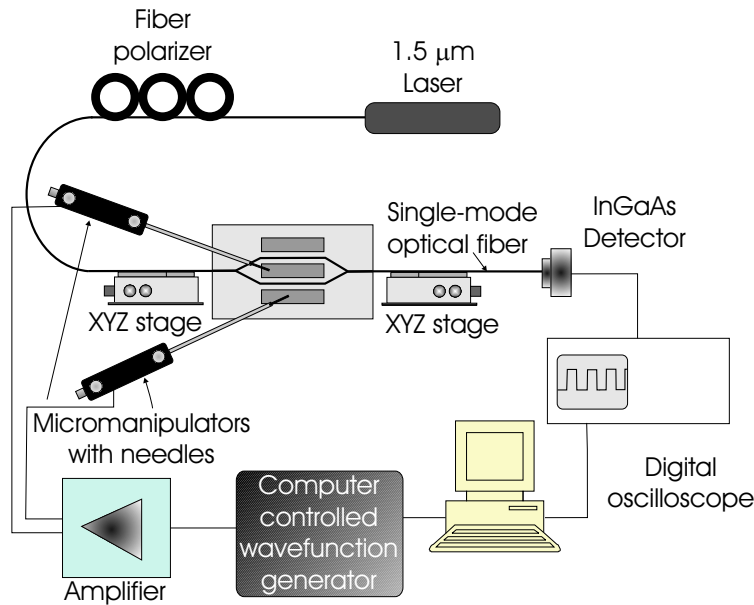


Figure 4.15: The experimental setup for frequency response measurements.

A wave function generator gives a square signal with adjustable amplitude, dc offset and frequency. This signal is coupled to a 10 x voltage amplifier with relatively high output voltage range of 0 - 100 V and an output impedance of 50 ohm. The amplified signal drives the optical modulator. The signal from the light detector is visualized and recorded with a digital oscilloscope. A computer program scans the frequency range of the generator and records the signal from the oscilloscope. A data set containing the output intensity of the modulator versus frequency is obtained.

4.4 Epitaxial BaTiO₃

4.4.1 c-axis films

Film growth and characterization

c-axis oriented BaTiO₃ films were grown by pulsed laser deposition (PLD) using a KrF excimer laser with the following characteristics: wavelength 248 nm, pulse length 20 ns, repetition rate 10 Hz, fluency of 2.5 J/cm². The substrate, single side polished MgO (100) 10x10x1 mm³ was placed 4 cm from the target on a SiC resistive heater. The BaTiO₃ target was a cylinder containing sintered single-phase barium titanate. BaTiO₃ films were grown at a substrate temperature of around 800 °C under an oxygen atmosphere of 2x10⁻³ mbar. The substrate temperature was measured by an IR pyrometer. The film thickness is about 1 μm in accordance with the conditions necessary for fabricating single mode ridge waveguides discussed in section 4.2.2.

The stoichiometry of the films was verified by Rutherford backscattering (RBS) measurements. Comparing the simulated and measured spectra, we found that Ba:Ti ratio is 1:1. The oxygen concentration in the film is more difficult to determine by RBS due to the low atomic mass of oxygen. The channelling spectrum (Figure 4.16) revealed a low value of the minimum yield of $\chi_{min} = 2\%$. This is a typical value for single crystals [36] which attests the crystalline quality of the BaTiO₃ films.

X-ray diffraction measurements were performed for characterizing the films. A $\theta/2\theta$ scan of an 1 μm thick BaTiO₃ film on MgO is shown in Fig. 4.17 a. The x-ray spectrum contains only peaks corresponding to (00 l) reflections of BaTiO₃ and substrate peaks, demonstrating that the films are highly oriented, with the c axis perpendicular to the film plane. The average out-of-plane lattice parameter calculated from the two-theta values of the BaTiO₃ peaks is $c = 4.048 \text{ \AA}$, which is close to the c-axis parameter of bulk tetragonal BaTiO₃ (4.033 Å) [37].

By tilting the sample at a fixed angle during a conventional $\theta/2\theta$ scan, the lattice spacing of the (103) planes can be measured (Fig. 4.17 b). Thus, the lattice constant parallel to the surface (in-plane) can be calculated. An in-plane value of 3.999 Å has been estimated, very close to the value of the a axis reported for powder tetragonal BaTiO₃ (3.994 Å) [37].

The rocking curve of the (002) BaTiO₃ reflection was measured and the full width at half maximum (FWHM) is $\Delta\omega = 0.45^\circ$, indicating well-oriented BaTiO₃ films (Fig. 4.17 c).

To investigate the in-plane texturing, the Schulz reflection method [26] with a three axis diffractometer was used. An off-axis scan of the BaTiO₃ (202)

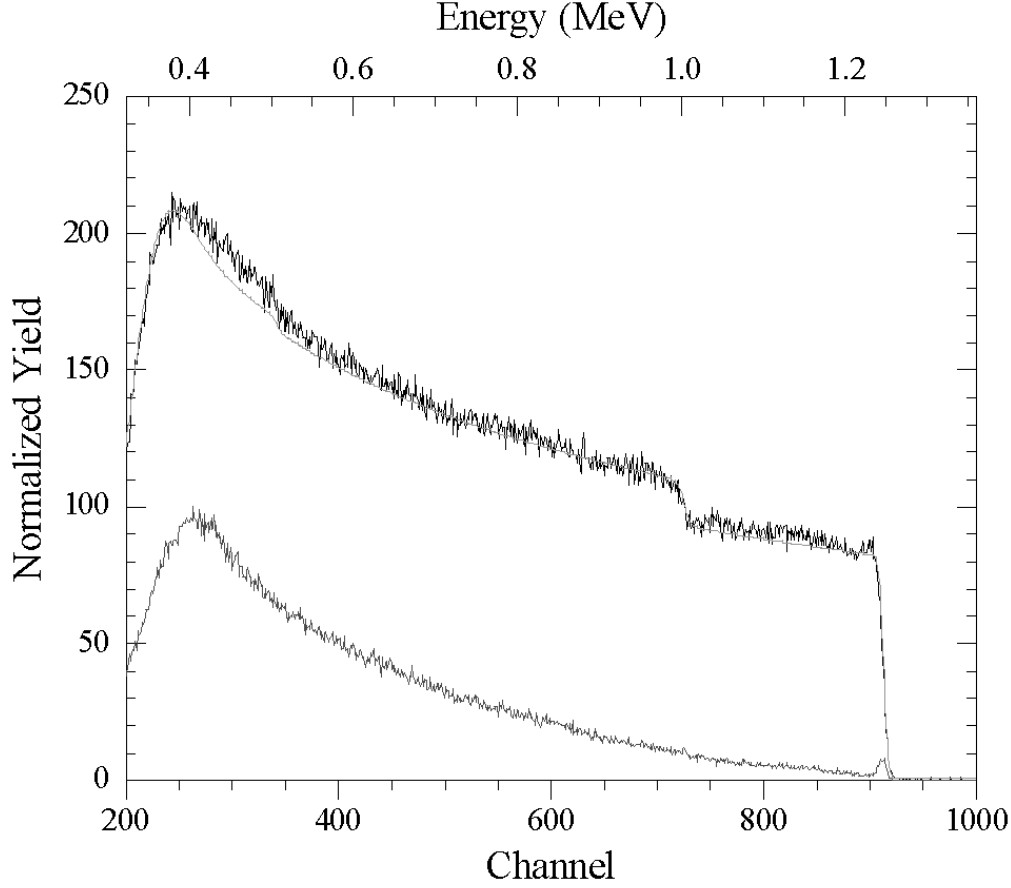


Figure 4.16: RBS/ ion channeling spectra of an 1 μm thick c-axis oriented BaTiO₃ film on MgO.

was performed to determine the in-plane alignment. The ϕ scan presented in Fig. 4.17 d confirms the in-plane epitaxy of the BaTiO₃ films.

The surface morphology is an important factor for thin film waveguide applications, rough surfaces leading to high scattering losses. As shown by Fork *et al.* [38], a surface root mean square roughness (rms) of about 1 nm or below would be desirable for waveguiding. Our PLD grown BaTiO₃ films on MgO with a thickness of 1 μm shows a rms roughness of 0.98 nm, as measured by atomic force microscopy (AFM). Figure 4.18 shows an AFM image of a 3 x 3 μm^2 area of an 1 μm thick c-axis oriented BaTiO₃ on MgO film.

A BaTiO₃ film with a refractive index of $n_{\text{BTO}} \simeq 2.4$ situated between the MgO substrate with a refractive index of $n_{\text{MgO}} \simeq 1.7$ and the air ($n_{\text{air}} \simeq 1$) forms a planar waveguide. Thus, a prism coupling set-up as described in section 4.3 is a proper tool for optical characterization of the film. The

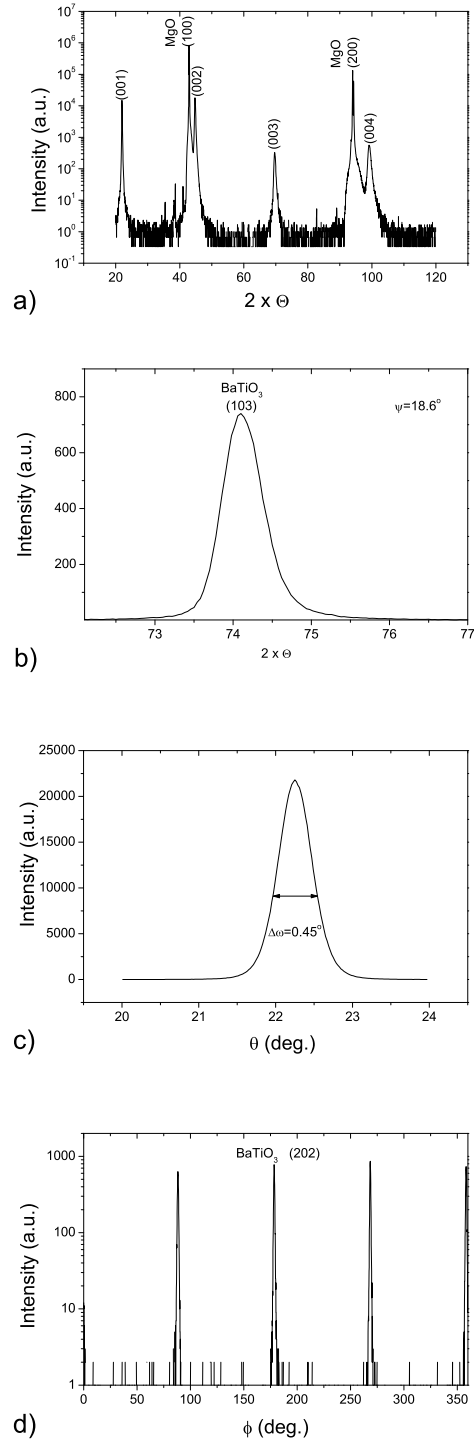


Figure 4.17: a) Conventional x-ray diffraction pattern of an $1 \mu\text{m}$ thick BaTiO_3 film on MgO (100); b) two theta scan of BaTiO_3 (103) at $\psi = 18.6^\circ$; c) rocking curve of (002); d) ϕ scan of (202).

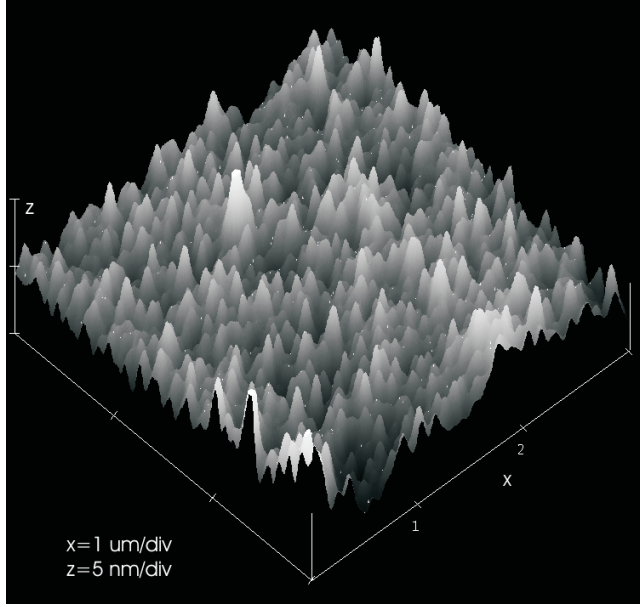


Figure 4.18: AFM image of a $3 \times 3 \mu\text{m}^2$ c-axis oriented epitaxial BaTiO₃ film on MgO. The film thickness is $1 \mu\text{m}$, the rms roughness is 0.98 nm .

in-plane and the out-of-plane refractive indices n_{TE} , n_{TM} were measured. The values n_{TE} , n_{TM} of the PLD deposited BaTiO₃ films depend on the film thickness and the substrate temperature during the deposition process. Beckers *et al.* [39] showed that in-plane refractive index (n_{TE}) is more sensitive to the variation of the film thickness than n_{TM} . The films used for Mach-Zehnder modulators have the refractive indices $n_{TE} = 2.351 \pm 0.002$ and $n_{TM} = 2.324 \pm 0.002$ measured at 632.8 nm wavelength, and a birefringence of $\Delta n = n_{TM} - n_{TE} = -0.027$. At $1.5 \mu\text{m}$ wavelength we measured $n_{TE} = 2.252 \pm 0.002$ and $n_{TM} = 2.247 \pm 0.002$, $\Delta n = -0.005$. The loss coefficient of the planar waveguides for good quality films at 633 nm wavelength are between 2 and 5 dB/cm . Figure 4.19 shows the result of the loss measurement for a planar waveguide on c-axis BaTiO₃ film on MgO.

We have also grown c-axis oriented epitaxial BaTiO₃ films on GdScO₃(110) and LaAlO₃ substrates. The films grown on GdScO₃ show a lower loss coefficient, typically below 2 dB/cm at 633 nm [40].

Electro-optic characterization

Starting from c-axis epitaxial grown BaTiO₃ films with a thickness of approx. $1 \mu\text{m}$, Mach-Zehnder modulators have been fabricated as described in section 4.2. With this electrode geometry (lateral electrodes) and c-axis oriented

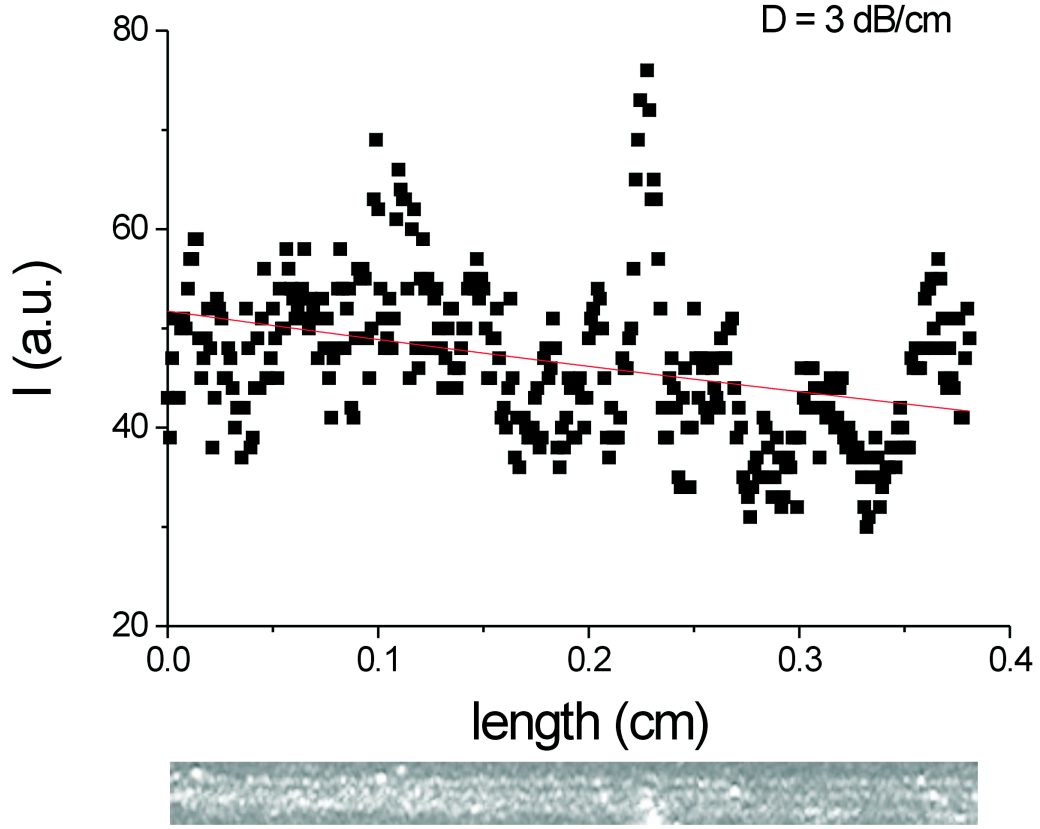


Figure 4.19: Loss measurement for a c-axis epitaxial BaTiO_3 film on MgO . The loss coefficient is about 3 dB/cm.

films, the external driving electric field is perpendicular to the optical axis of the film. The theoretical modelling for this case is presented in section 3.5. The experimental setup used for measuring the electro-optic response of the modulators has been shown in section 4.3. The input light is linear polarized, polarization state being adjusted by a fiber polarizer and a Glan-Thompson cross-polarizer. In our experiments we used an in-plane polarized laser beam. The output of the modulator is connected to another optical fiber which leads the optical signal to a silicon detector. A computer program scans the driving voltage range (typically 0 V - 100 V) and reads the signal from the detector. Figure 4.20 shows the optical output intensity versus the applied voltage.

The upper scale of the graph shows the modulating electric field across the waveguide. The experimental data are plotted with squares. On the same graph the result of the modelling is plotted, as discussed in section 3.5 with

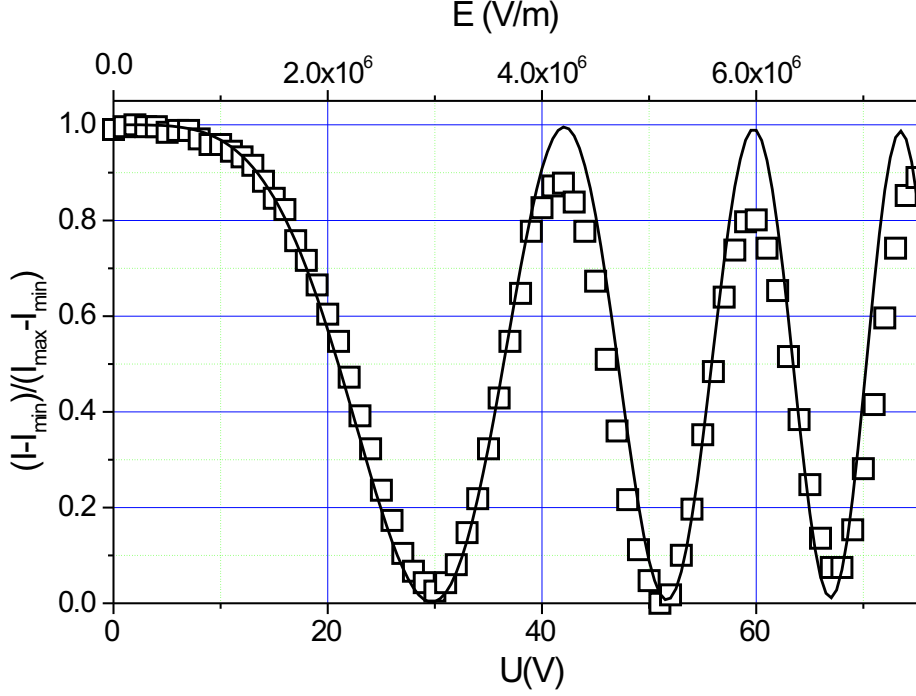


Figure 4.20: Response of the modulator at 633 nm wavelength. The squares are the experimental data and the line is the theoretical response with $r_{51}^{eff} = 87$ pm/V.

a line. The parameters used for the theoretical curve were: wavelength $\lambda = 633$ nm, the ordinary and extraordinary refractive indices $n_o = 2.348$ and $n_e = 2.322$, the length of the electrodes $l = 3$ mm, separation between electrodes $d = 10$ μm , in-plane polarized light $\psi = 0$ degrees. The value of the electro-optic coefficient $r_{51}^{eff} = 87$ pm/V has been adjusted for the best fit with the experimental data. As it can be seen from the graph, the experimental results are in good agreement with the theoretical modelling. Gill *et al.* [41, 42] reported an effective electro-optic coefficient of 50 pm/V for a channel waveguide electro-optic modulator in epitaxial BaTiO₃ grown by low-pressure metalorganic chemical vapor deposition, which is in agreement with our results.

Similar experiments were performed for measuring the electro-optic response

at 1550 nm wavelength. The He-Ne laser has been replaced with a semiconductor cw laser at 1550 nm, the single mode optical fibers and the fiber polarizer have been replaced by similar components designed for 1550 nm wavelength and the silicon detector has been replaced by an InGaAs detector sensitive in infrared range. The result of the infrared measurements is shown in Fig. 4.21.

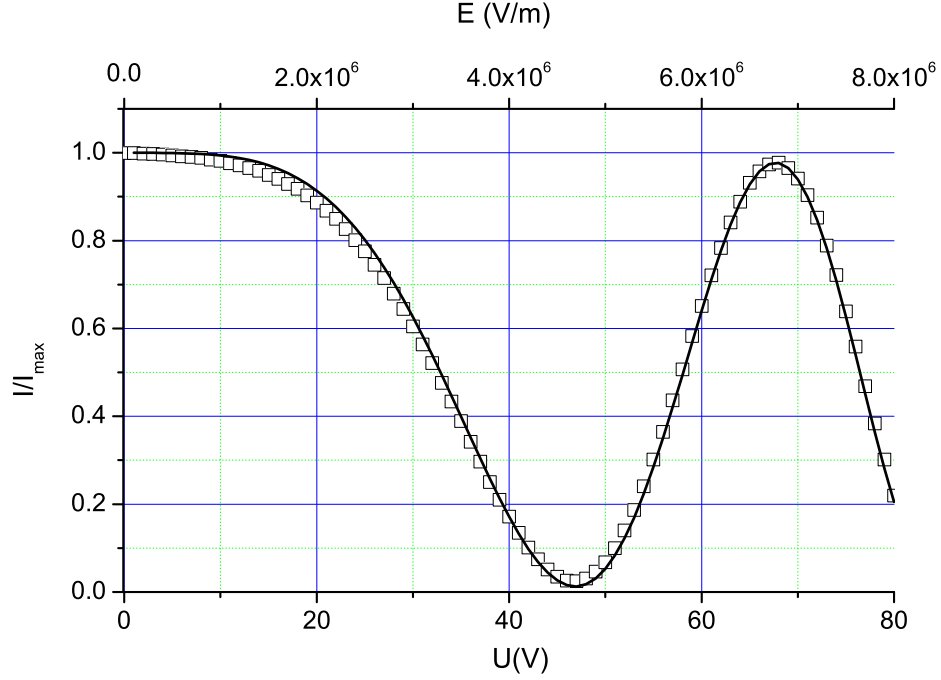


Figure 4.21: Response of the modulator at 1.5 μm wavelength.

As discussed in section 3.5, from the theoretical modelling of c-axis Mach-Zehnder modulators with the applied electric field perpendicular to the optical axis in transverse geometry (driving field perpendicular to the beam propagation direction), the induced phase shift has a quadratic dependence with the applied field. This was checked experimentally by measuring the output intensity while applying opposite electric fields on both arms of the modulator $E(t)$, $-E(t)$. The result is shown in Fig. 4.22. Three curves are recorded, one with $E(t)$ applied to first arm, another with $-E(t)$ applied to the other arm and the last one with both $E(t)$, $-E(t)$ applied simultaneously to both arms of the modulator. No significant change in the output has been observed when $E(t)$, $-E(t)$ have been applied simultaneously, as predicted

by the modelling.

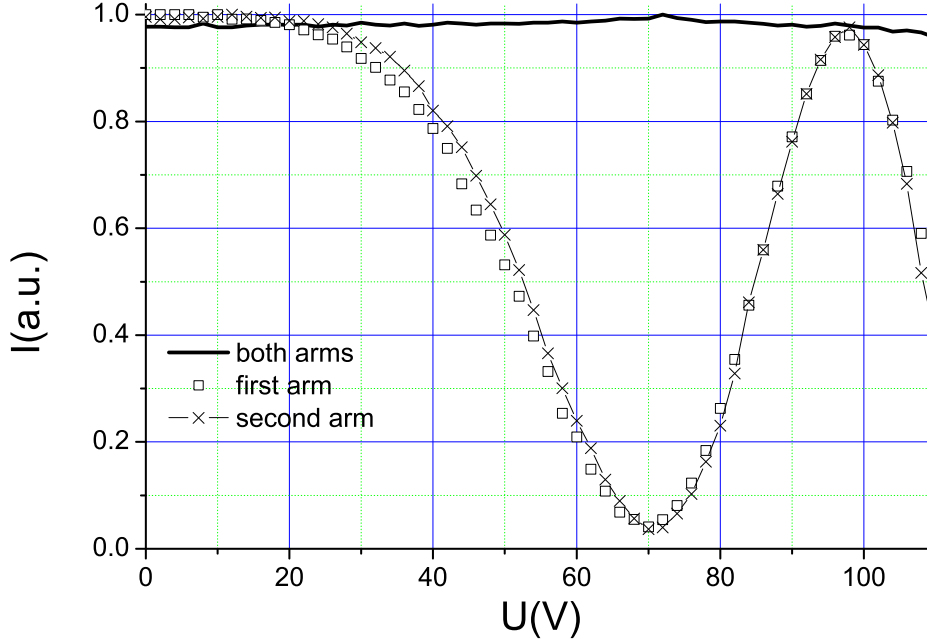


Figure 4.22: Response of the modulator for $E(t)$ applied to one arm (squares), $-E(t)$ applied to the other arm (crosses) and both applied simultaneously (line). Measurements were performed at $1.5 \mu\text{m}$ wavelength.

We have measured the modulation depth versus frequency at 1550 nm by driving the device with a square wave electrical signal of 21 V_{p-p} (at a bias of 46 V). The result is shown in Fig. 4.23. The performance is very stable over the entire tested frequency range up to 1 MHz .

Packaging

In order to mount the modulators and attach optical and electrical connectors, Mach-Zehnder modulator with large electrode pads were fabricated. Thus, we used wire bonding (Ag wires, $20 \mu\text{m}$ diameter) to connect the electrodes to an electrical connector. As input and output optical connectors we used two optical fibers with standard FC connectors at one end. The other end was prepared to be glued direct to waveguide. We used a fiber optic stripping tool and a fiber optic cleaver. The cleaved ends were cleaned with acetone and propanol. The input fiber is a polarization maintaining

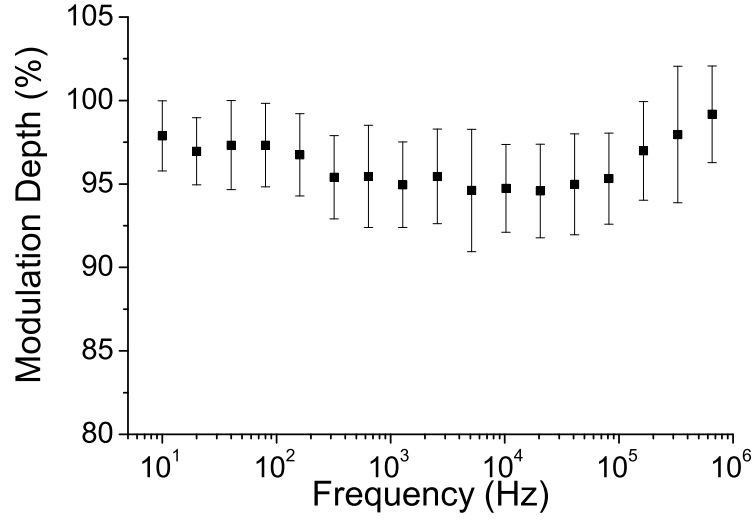


Figure 4.23: Modulation vs frequency (21 V_{p-p} modulating square signal, 46 V_{dc} bias, 1550 nm light).

fiber and the output fiber is a single mode fiber at 1.5 μm . The fibers were connected to the waveguide using the set-up for electro-optic measurements (section 4.3). After the alignment of the fibers to the waveguide (adjusting of the nanopositioning tools for maximum output signal), the fibers were fixed with an UV-curing optical adhesive. The adhesive is transparent in the whole visible and near infrared range, it has a refractive index of 1.5 and ensures a good mechanical fixing. Figure 4.24 shows a picture of a packaged BaTiO₃ thin film Mach-Zehnder modulator.

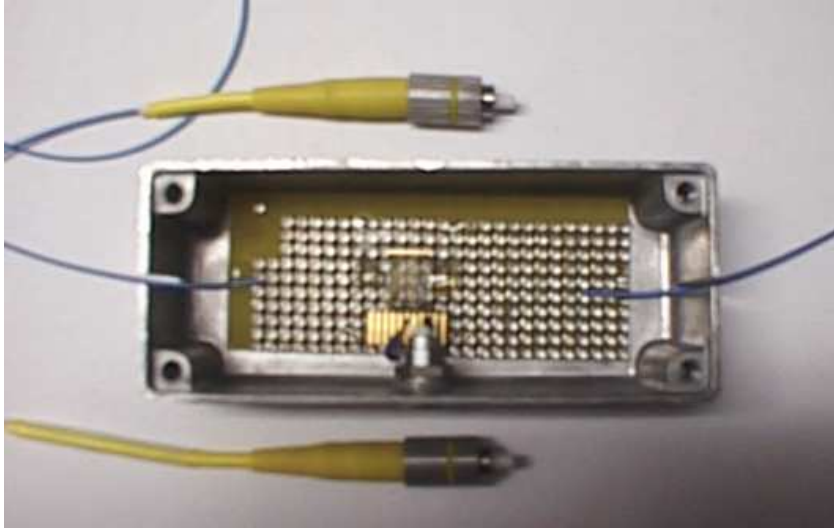


Figure 4.24: Packaged BaTiO₃ thin film Mach-Zehnder modulator.

4.4.2 a-axis films

Film growth and characterization

Depending on the laser energy, oxygen pressure, substrate temperature during deposition, film thickness, the epitaxial BaTiO₃ films deposited by pulsed laser deposition on MgO substrates may have c-axis or a-axis orientation. a-axis oriented epitaxial BaTiO₃ films were reported by several authors on MgO and SrTiO₃ substrates [43, 44]. Epitaxial BaTiO₃ films with a-axis orientation grown by laser molecular beam epitaxy have also been reported [45]. The mismatch in thermal expansion coefficient and lattice constants also plays a role in the film orientation [45, 43]. One of the most important factors in determining the crystallographic orientation of the PLD deposited films is the kinetic energy of the ablated particles [46]. The kinetic energy depends strongly on the laser energy and oxygen pressure. High oxygen pressure increases the collisions between the ablated particles and the oxygen species and the thermal vibration of the ablated particles arriving the substrate becomes weaker.

In our experiments we increased the substrate temperature and reduced the laser energy in comparison with the c-axis oriented films. Table 4.3 shows the deposition parameters for the a-axis films and c-axis films.

The composition of the films was analyzed by Rutherford Backscattering Spectrometry. The random spectrum (Fig. 4.25) gives a Ba:Ti ratio of 1:1. From the channelling spectrum we found a good crystallinity of the films,

Deposition parameter	c-axis films	a-axis films
Substrate temperature	800 °C	850 °C
Laser energy	1100 mJ/pulse	≤ 300 mJ/pulse
Oxygen Pressure	2×10^{-3} mbar	2×10^{-3} - 6×10^{-3} mbar
Repetition rate	10 Hz	25 Hz

Table 4.3: Deposition parameters for PLD deposited c-axis and a-axis films.

with a minimum yield χ_{min} of 1 % measured at the barium signal.

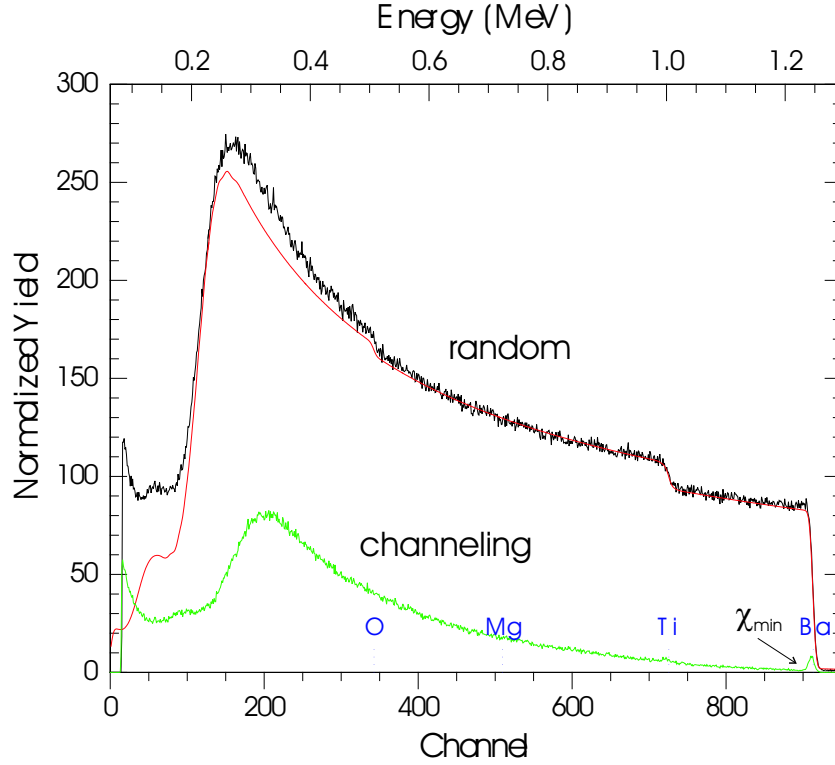


Figure 4.25: RBS/channelling spectra of an 1 μm thick BaTiO_3 a-axis film. Minimum yield is $\chi_{min} = 1\%$.

From the XRD normal $\theta/2\theta$ scan (Fig. 4.26), an out-of-plane lattice constant of 4.01 Å was determined, close to the a lattice constant of the tetragonal BaTiO_3 . The diffraction patterns show no diffraction peaks from impurity phases or randomly oriented grains, which means that the thin films are single phase BaTiO_3 . By tilting the sample at an angle $\psi = 45.5^\circ$ during a conventional $\theta/2\theta$ scan, the lattice spacing of the (101), (202) and (303) planes was measured. This allow us to determine the in-plane lattice constant

of the a-axis films, which is $c = 4.032\text{\AA}$. As shown in Fig. 4.26c the XRD ω rocking curve displays a full width at half maximum (FWHM) of 0.29° for the (002) peak of the BaTiO₃. The narrow peaks of the BaTiO₃ films indicate that the film has a very high degree of crystallinity. The in-plane misorientation of the a-axis films was evaluated by XRD ϕ scans of the (103) peak. The result is shown in Fig. 4.26d. The peaks in the scan are spaced by 90° and no random peaks occur, indicating that no measurable in-plane misorientation exists in the a-axis oriented BaTiO₃ films.

Table 4.4 contains the lattice parameters of the of the a-axis and c-axis oriented BaTiO₃ films epitaxially grown on MgO measured by x-Ray diffraction.

Lattice parameter	a-axis films	c-axis films	bulk BaTiO ₃
c [\AA]	4.032	4.048	4.0361
a [\AA]	4.010	3.999	3.9920

Table 4.4: Lattice parameters of epitaxial a-axis and c-axis oriented films on MgO in comparison with lattice parameters of bulk BaTiO₃.

Using an intermediate laser energy of 420 mJ, "pseudo-cubic" BaTiO₃ films were obtained at a substrate temperature of 750°C . XRD measurements showed that the in-plane and the out-of plane lattice constants have approximately the same value of 4.010 \AA . The result of the XRD measurements were confirmed by optical measurements which showed almost no birefringence of the "pseudo-cubic" films.

The in-plane and the out-of-plane refractive indices of the a-axis films (n_{TE} and n_{TM}) were measured with a prism coupling setup. Our a-axis films have $n_{TE} = 2.353$ and $n_{TM} = 2.365$ and a birefringence $\Delta n = n_{TM} - n_{TE}$ of 0.012. This value is slightly smaller than for the c-axis films ($\Delta n = -(0.018 - 0.026)$) and has an opposite sign. Table 4.5 contains the measured refractive indices of the a-axis film in comparison with the c-axis films.

parameter	c-axis films	a-axis films
n_{TE}	2.351	2.353
n_{TM}	2.324	2.365
$\Delta n = n_{TE} - n_{TM}$	-0.027	0.012

Table 4.5: The in-plane and out-of plane refractive indices of the a-axis films and c-axis films.

Optical loss measurements of the planar waveguides formed by the a-axis film on MgO substrate were performed with the prism coupling setup. Figure 4.27

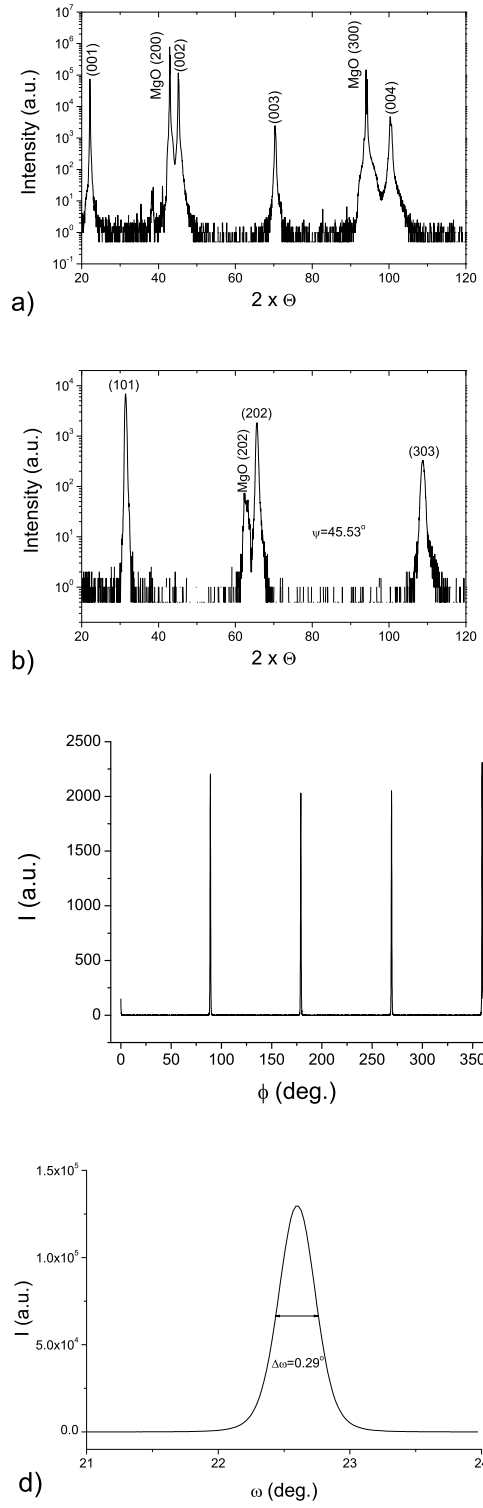


Figure 4.26: a) Conventional x-ray diffraction pattern of an 1 μm thick epitaxial a-axis oriented BaTiO₃ film on MgO (100); b) two theta scan of BaTiO₃ (101), (202) and (303) reflections at $\psi = 45.5^\circ$; the rocking curve of (002) peak of BaTiO₃; the ϕ scan of the (103) peak of BaTiO₃.

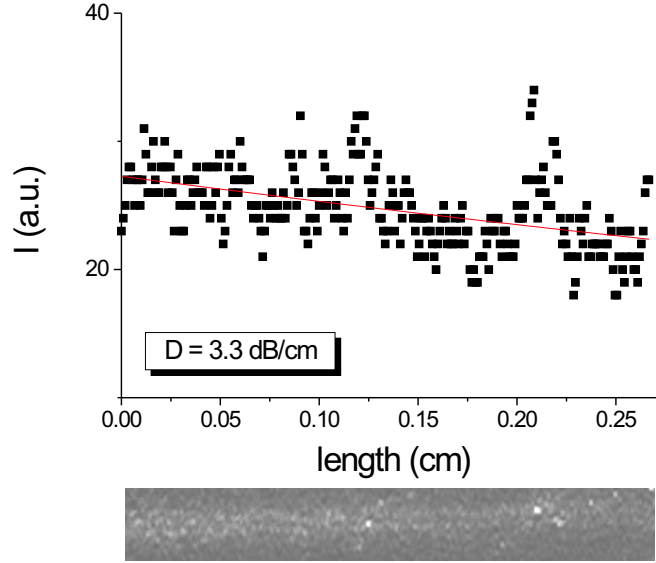


Figure 4.27: Loss measurement for an a-axis epitaxial BaTiO₃ film on MgO.

shows the intensity of scattered light of the TE₀ mode versus length. A loss coefficient of about 3.5 dB/cm was measured.

Electro-optic characterization

Mach-Zehnder modulators with similar design as in case of c-axis modulators were fabricated, with electrode length of 3 mm and electrodes spacing of 10 μm . The rib waveguides having a rib height of 70 nm and a rib width of 2 μm maintain single mode propagation at both investigated wavelengths, 633 nm and 1550 nm. The modulators have also a transverse geometry like in the case of c-axis films but the external electric field is applied along the optical axis of the film. The same experimental set-up described in section 4.3 has been used for measuring the response of the modulator. Figure 4.28 shows the output intensity of the modulator while changing the external applied electric field at 632.8 nm wavelength. On the same graph is plotted a fit of the experimental data with the theoretical modelling given by eq. 3.45. An additional phase shift has been added to one arm of the modulator in the simulations to compensate the asymmetries due to fabrication and film imperfection.

A half wave voltage $V_\pi = 6.3 \text{ V}$ has been measured at this wavelength. For low modulating fields (up to $1.5 \times 10^6 \text{ V/m}$) we find $r_{33}^{eff} = 21 \text{ pm/V}$. For electric fields in the range from 2×10^6 to $3 \times 10^6 \text{ V/m}$ the value of this

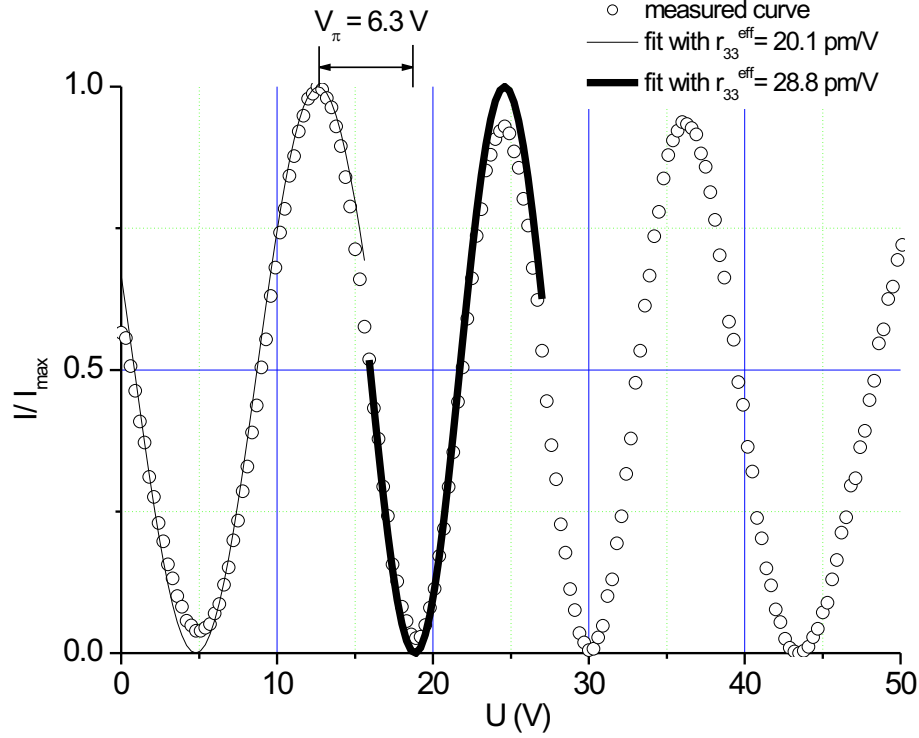


Figure 4.28: Performance of Mach-Zehnder modulators made from a-axis films at 633 nm wavelength.

coefficient increases to $r_{33}^{eff} = 28$ pm/V. For high applied electric fields (3.5×10^6 to 5×10^6 V/m) r_{33}^{eff} decreases again. The increase of r_{eff} for medium fields may be explained by some poling of the film due to the applied field. The decrease of r_{eff} for high applied fields is probably due to leakage currents. The a-axis BaTiO₃ modulators were measured also at 1550 nm, the wavelength for fiber optic communication. A half wave voltage of $V_\pi = 9.5$ V has been measured. According to eq. 3.47 from the modelling section, this value of V_π corresponds to an effective Pockels coefficient of $r_{33}^{eff} = 42$ pm/V. The modulation depth measured at $1.5 \mu\text{m}$ is 99.1 %, corresponding to an extinction ratio $E_r = 10 \log_{10} \frac{I_{max}}{I_{min}}$ of 20.5 dB (see Fig. 4.29). The output fiber was removed from the setup and replaced with a microscope objective and a CCD camera. Thus, the images of the "on" and "off" states of the modulator were taken (Fig. 4.30).

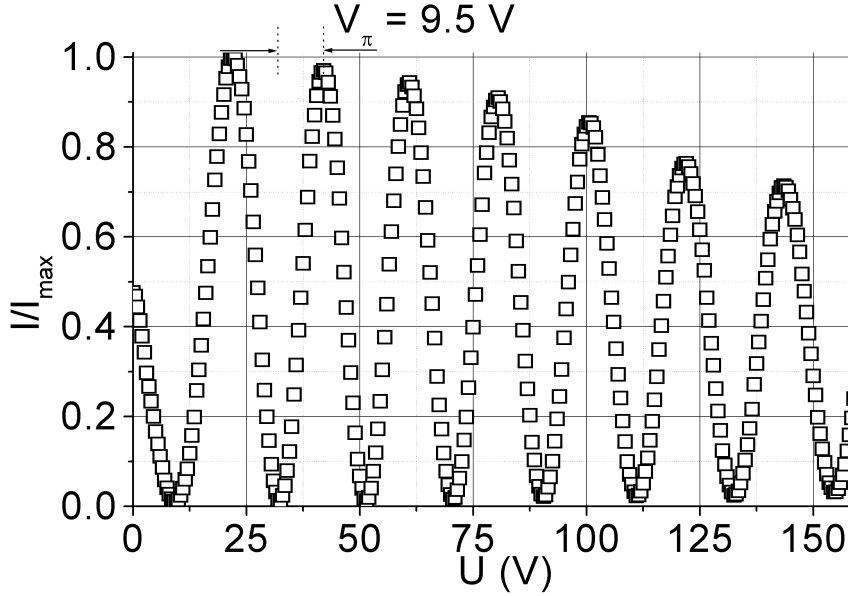


Figure 4.29: Response of the a-axis modulator at 1.5 μm wavelength.

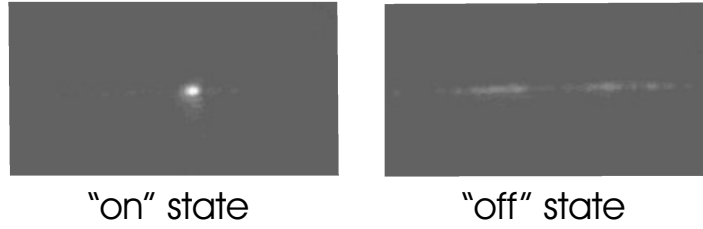


Figure 4.30: Photographs of the "on" and "off" states of the modulator taken with a microscope objective and a CCD camera at 1.5 μm .

4.5 Polycrystalline BaTiO₃ Mach-Zehnder modulators

As a next step towards the integration of ferroelectric BaTiO₃ thin films on different substrates, we have modified the growth conditions by lowering the growth temperature to study polycrystalline BaTiO₃ thin films. A series of BaTiO₃ films on MgO were grown by pulsed laser deposition and the substrate temperature range during the deposition was 250 °C - 800 °C. For this wide range of temperatures, crystalline, polycrystalline and amorphous layers were produced. The best optical quality (low loss) of the polycrystalline films was achieved for a substrate temperature during the deposition of about 400 °C and an oxygen pressure of 2×10^{-3} mbar.

4.5.1 Film growth and characterization

The polycrystalline BaTiO₃ films were deposited on MgO(001) substrates using the Pulsed Laser Deposition (PLD) technique. The films were grown at 10 Hz repetition rate of the KrF excimer laser and 1 J per pulse laser energy. The beam is focused on a rotating target in a line-focus of 40 x 0.5 mm². The cylindrical target of 2 cm diameter consists of single phase BaTiO₃ powder which has been pressed and sintered. The deposition process takes place under an oxygen pressure of 2×10^{-3} mbar and a substrate temperature of around 400 °C.

Structural characterization

The composition and the thickness of the sample were measured by Rutherford Backscattering Spectroscopy (RBS). The Ba: Ti ratio is 1: 1 within the resolution, in accordance with the initial target composition.

In RBS/Channeling experiments, no channelling in the Ba signal could be detected, indicating that the BaTiO₃ films are not preferentially textured on the MgO substrate.

Grazing incidence X-Ray Diffraction (XRD) measurements were performed. They confirmed, that the films are polycrystalline. Several XRD grazing incidence scans were performed at different angles of incidence (0.5°, 1°, 1.5° and 2°). No shift or additional line appeared in the spectra denoting that the structure does not change at different depths. Figure 4.32 displays the XRD patterns of the BaTiO₃ films taken at grazing incidence, with an angle of incidence of 2 degrees. The lines are broadened, with a FWHM between 0.32 and 0.9 degrees. Therefore it is difficult to distinguish between tetragonal and cubic phases of BaTiO₃ [47].

A film grain size of 19 nm has been estimated using the Dehlez method based on x-ray line shape analysis [48]. The grain size of the crystallites plays an important role for optical applications. An average grain size below $\lambda_0/10$ is well suited for optical devices operating at vacuum wavelength λ_0 . PE-MOCVD grown polycrystalline BaTiO₃ films on Si partially textured in the [100] direction were reported by Buskirk *et al.* [49].

The surface morphology of the films is very important for optical waveguide applications. The surface roughness was measured by atomic force microscopy (AFM). Figure 4.33 shows an AFM image of an $1 \times 1 \mu\text{m}^2$ area of a 1 μm thick polycrystalline BaTiO₃ film. The surface appears to be very flat, with a maximum variation in height (peak-to-valley roughness) of 6.3 nm. The root mean square (rms) roughness for the measured area is 0.9 nm, comparable with the rms roughness of 1.1 nm of the epitaxial BaTiO₃ films

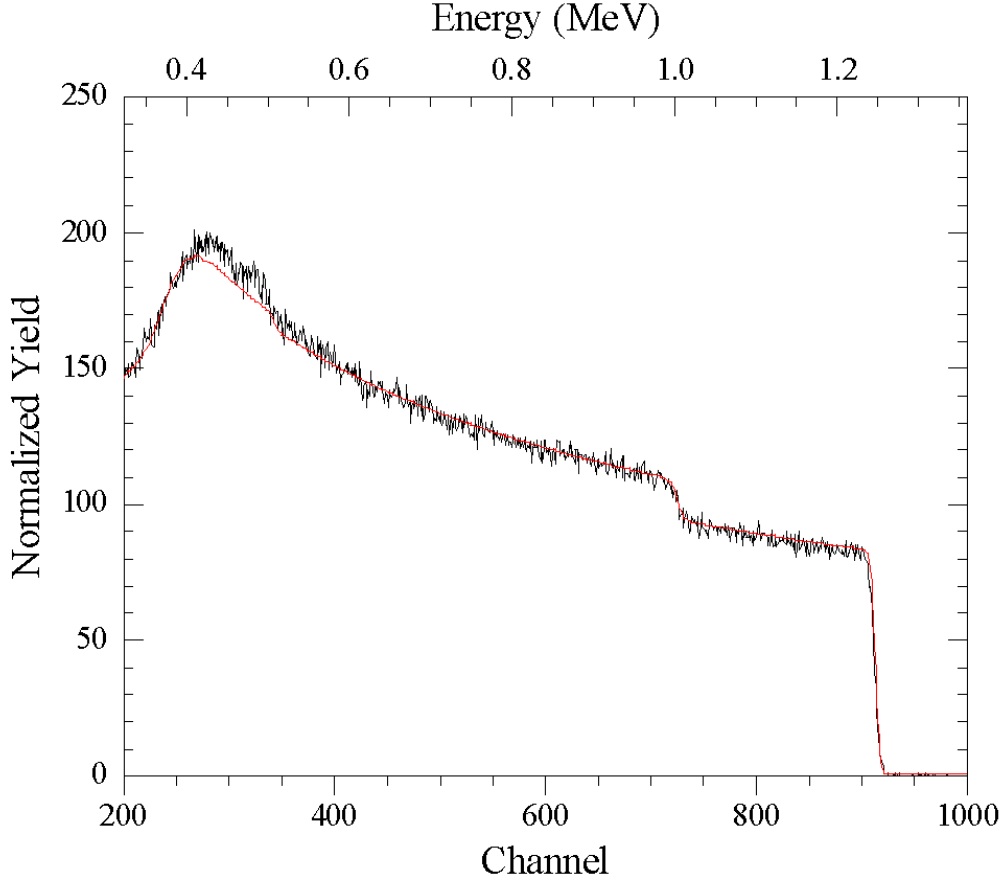


Figure 4.31: RBS spectrum of a 1 μm thick polycrystalline BaTiO₃ film deposited on MgO.

on MgO as reported by Beckers *et al.* [39].

4.5.2 Optical and electro-optical characterization

The in-plane and the out-of-plane refractive indices n_{TE} , n_{TM} of the BaTiO₃ polycrystalline films with the thickness of around 1 μm have been measured using a prism coupling setup [35] and the values measured at 633 nm wavelength from the m-lines spectra are $n_{TE} = 2.316 \pm 0.002$ and $n_{TM} = 2.301 \pm 0.002$. The measurements have been repeated after rotating the sample with 90°. The same same values for the in-plane and out-of-plane refractive indices were obtained. The films are still birefringent, with a birefringence of 0.015 ± 0.002 .

Since cross-section SEM images (Fig. 4.34) of the film show a dense struc-

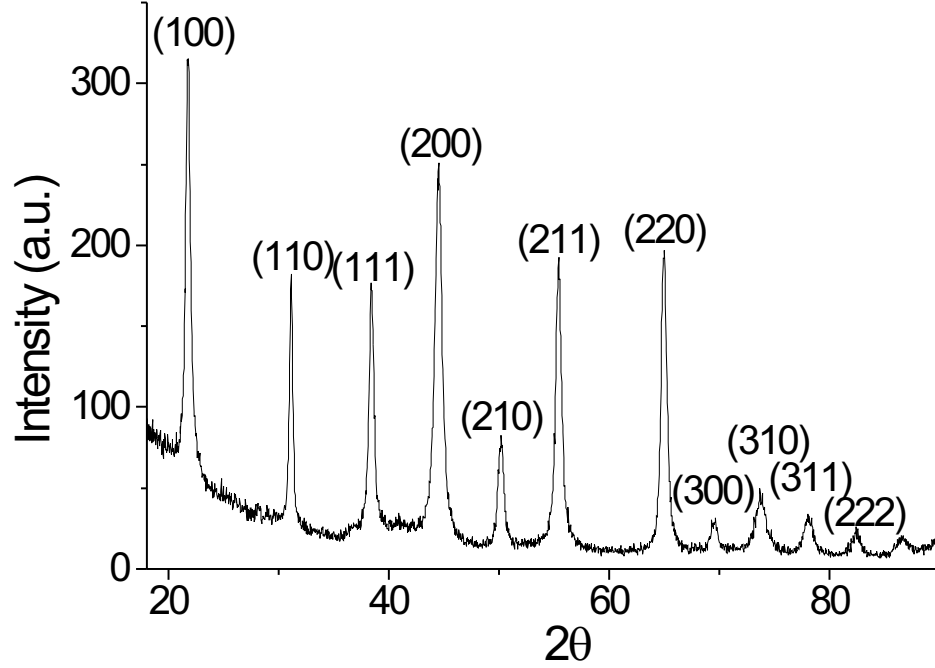


Figure 4.32: Grazing incidence XRD spectrum of as-grown polycrystalline BaTiO_3 deposited on MgO .

ture, without a columnar aspect, the relatively high birefringence may be attributed to a preferential orientation of the crystallites. Damping measurements were performed with the prism coupling setup, recording the scattered light with a CCD camera when the first mode (in-plane polarization) was coupled into the planar waveguide.

The measured loss coefficient of an $1\ \mu\text{m}$ thick BaTiO_3 polycrystalline film is about 4 dB/cm at 633 nm wavelength (see Fig. 4.35). This value is comparable but slightly higher than the values measured for the crystalline BaTiO_3 films on MgO : 2.9 dB/cm, reported by Beckers et al. (PLD grown) [39] and 4 ± 2 dB/cm as achieved by Gill et al. (MOCVD) [50, 41].

Ridge waveguides $3\ \mu\text{m}$ wide with a ridge step height of 70 nm were patterned on the films using standard optical lithography and ion beam etching, forming a Mach-Zehnder interferometer. Cr-Au electrodes with a length of 3 mm and a separation of $10\ \mu\text{m}$ were deposited besides the waveguides. The input and the output faces of the modulator have been cleaved. The in-plane polarized light was supplied by a cw laser (633 nm and 1550 nm wavelength) and was

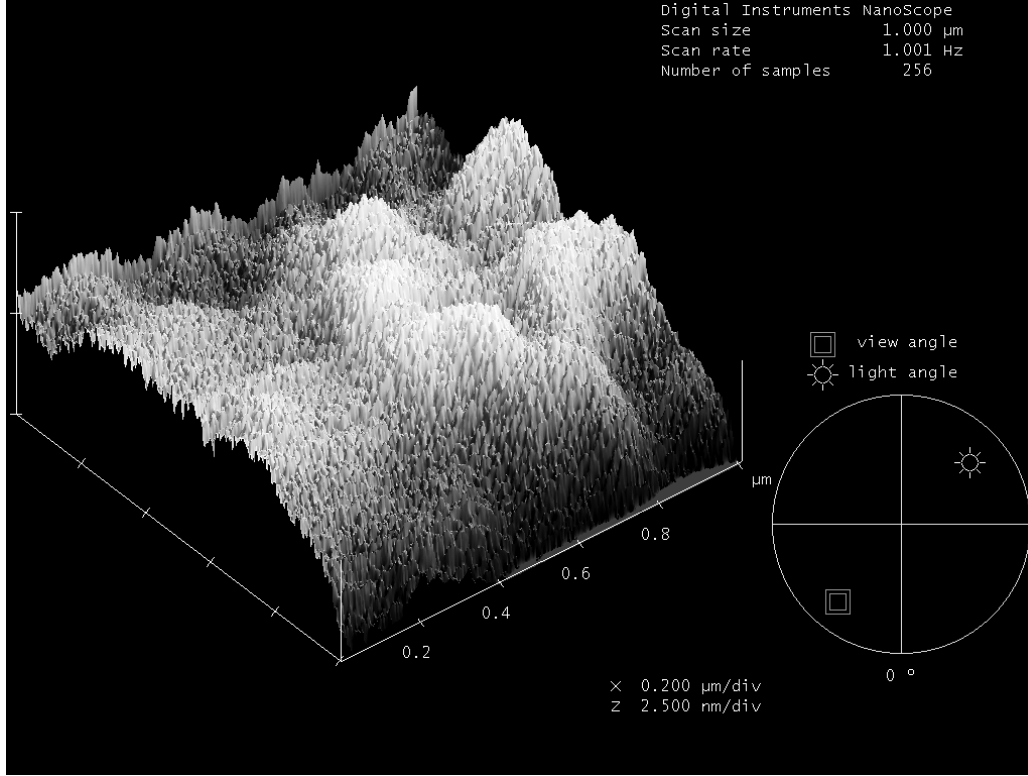


Figure 4.33: AFM image of 1 μm thick polycrystalline BaTiO₃ film on MgO. Scanned area is 1 x 1 μm^2 , $z = 2.5 \text{ nm/div}$.

end-fire coupled into the waveguide. For defining the polarization of the incoming light, a fiber polarizer has been used.

The positioning of the optical fibers to the input and output of the modulator has been done with two piezoelectric controlled micropositioning systems. The output is coupled to a photodetector.

We observed that the modulator exhibits a hysteretic behavior when we measured the output intensity versus the applied voltage, i.e. the scan with the voltage going up is shifted with respect to the scan with the voltage going down. This indicates a ferroelectric poling effect of the BaTiO₃ during the measurements. We analyzed this effect by first applying a step function electrical field of 6 V/ μm and recording the output intensity. Subsequently this field was switched off and the intensity recorded again. Thus, we found an exponential time response with a poling time constant of about $t_{\text{poling}} = 62 \text{ sec.}$ and a relaxation time constant of $t_{\text{relax.}} = 25 \text{ sec.}$ Figure 4.36 shows the optical output intensity versus time for a step like voltage applied to the electrodes.

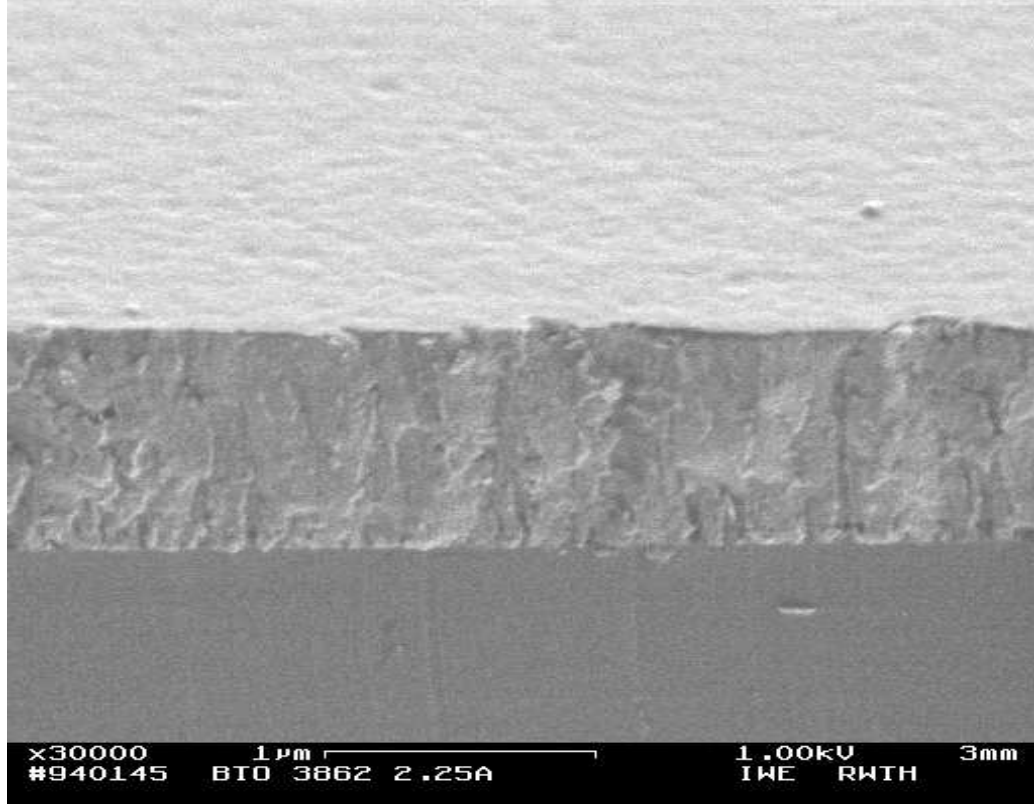


Figure 4.34: SEM image of 1 μm thick polycrystalline BaTiO_3 film on MgO . The sample was cleaved.

The electro-optic response of the modulator for 633 nm (line) wavelength and 1550 nm (dots) wavelength is shown in Fig. 4.37.

For the infrared measurement (1550 nm wavelength) the curve was taken with a voltage step of 0.5 V and a hold time between steps of 300 ms. This procedure implies, that the samples was subject to some poling during the measurement.

At relatively high electric fields up to $9 \text{ V}/\mu\text{m}$, the measured half wave voltage is $V_\pi \simeq 19 \text{ V}$. Thus, the corresponding effective electro-optic coefficient at $1.5 \mu\text{m}$ wavelength is about 22 pm/V .

A square wave voltage (frequency range 1 Hz - 1 MHz) was applied to the modulator and a stable operation point was found at 30 V_{p-p} and 60 V offset. This $V_\pi = 30 \text{ V}$ corresponds to an effective electro-optic coefficient $r_{eff} = 14 \text{ pm/V}$ at an applied electrical field of approx. $6 \text{ V}/\mu\text{m}$.

In order to decrease the operating voltage, identical optical modulators with smaller separation distance between the electrodes of $5 \mu\text{m}$ have been fabri-

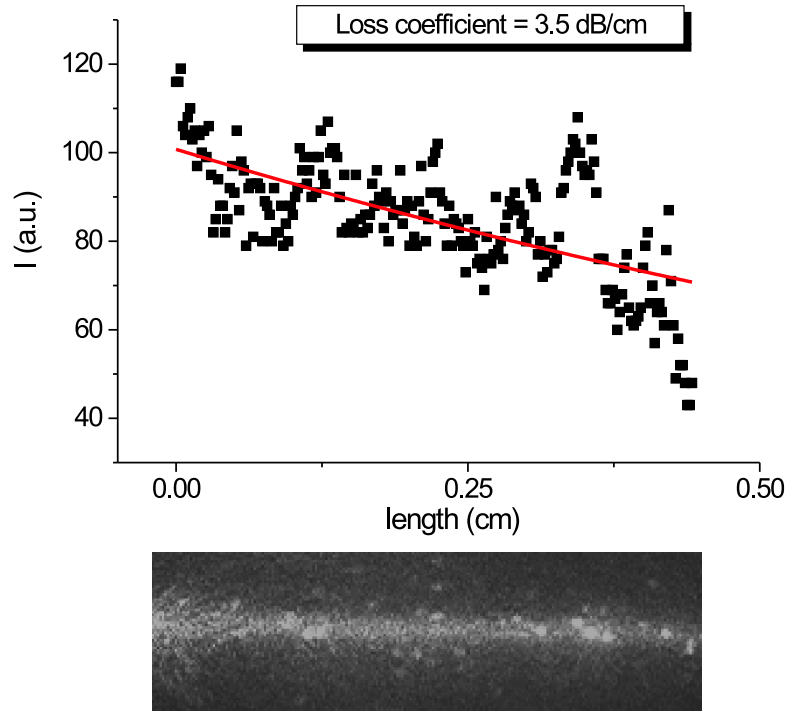


Figure 4.35: Loss measurement for an 1 μ polycrystalline BaTiO₃ film on MgO. The loss coefficient is about 4 dB/cm.

cated. Infrared measurements at 1550 nm wavelength show a $V_\pi = 17$ V at an applied electrical field of 10 V/ μ m (Fig. 4.38).

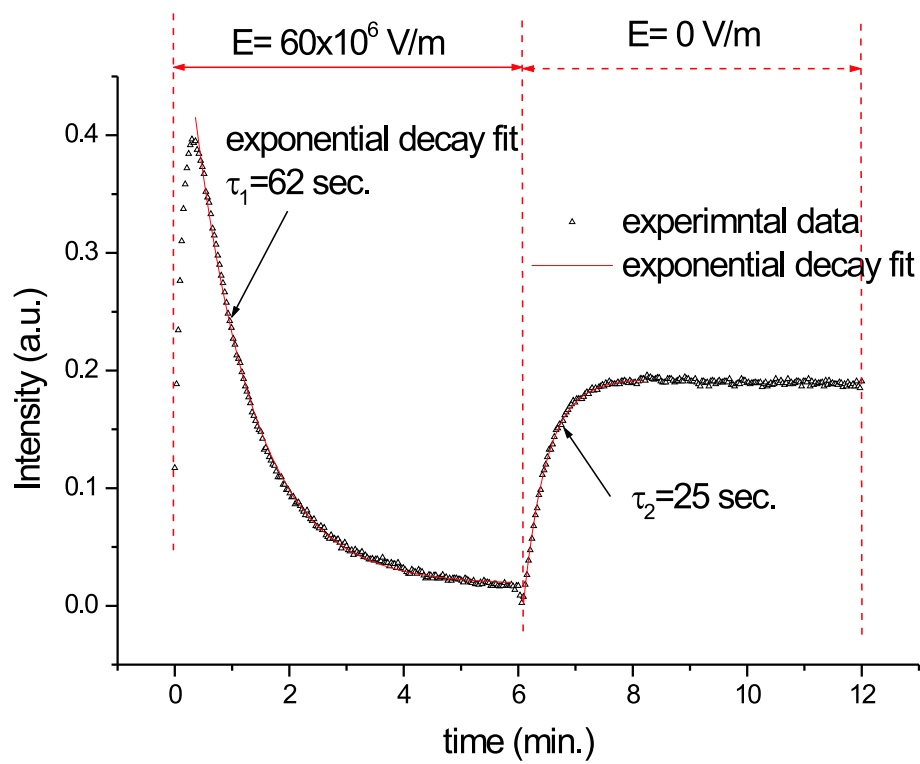


Figure 4.36: Poling and relaxation time response of a polycrystalline BaTiO₃ optical modulator.

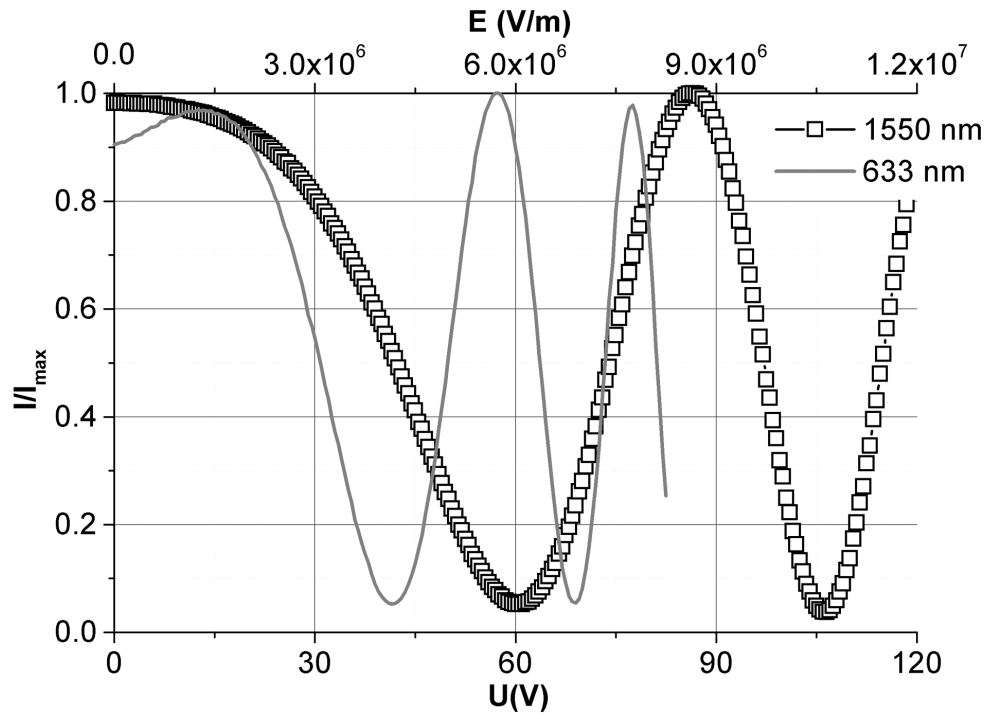


Figure 4.37: Response of the modulator while changing the applied voltage at 633 nm wavelength and 1550 nm wavelength. The voltage was applied to one arm of the modulator and the electrode spacing was 10 μm .

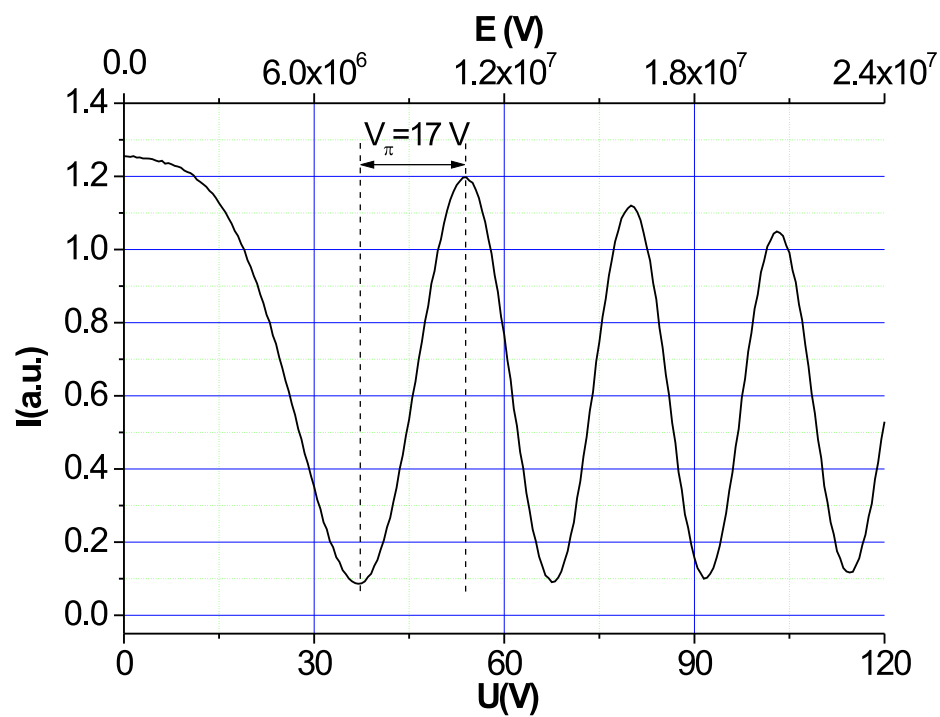


Figure 4.38: Response of polycrystalline BaTiO₃ modulator with 5 μm electrodes separation at 1.5 μm wavelength.

Chapter 5

Summary

The central task of this thesis is the structural, optical and electro-optical characterization of ferroelectric BaTiO₃ films grown by pulsed laser deposition and the realization of integrated optical Mach-Zehnder modulators based on these ferroelectric films. Within this work, the BaTiO₃ films with a thickness of about 1 μm were grown on MgO substrates forming planar optical waveguides. Pulsed laser deposition is a versatile thin film deposition technique which allows the growth of the epitaxial BaTiO₃ films on MgO with two different orientations of the films with respect to the substrate (c-axis and a-axis oriented films) by changing the deposition parameters (laser energy, substrate temperature, oxygen pressure), because the kinetic energy of the ablated particles depends strongly on laser energy and oxygen pressure. This modifies the growth conditions and the orientation of the ablated films. The composition of the film was analyzed by Rutherford backscattering. The ion/channelling experiments revealed a low value of the minimum yield χ_{min} for both c-axis and a-axis epitaxial films of about 1%, denoting a good crystallinity of the films.

X-ray diffraction measurements determined the film orientation and the in-plane and out-of-plane lattice constants. Thus, for the c-axis oriented films the in-plane and out-of-plane lattice parameters where $a = 3.999 \text{ \AA}$ and $c = 4.048 \text{ \AA}$. The a-axis films showed an in-plane lattice parameter of $c = 4.032 \text{ \AA}$ and an out-of-plane lattice parameter of $a = 4.010 \text{ \AA}$. The rocking curves of the (002) peaks with a FWHM of $\Delta\omega = 0.45^\circ$ for the c-axis films and $\Delta\omega = 0.29^\circ$ for the a-axis films attest the high degree of crystallinity of the epitaxial films. The in-plane and out-of plane refractive indices n_{TE} , n_{TM} were measured with a prism coupling setup. The a-axis films have a smaller and positive birefringence $\Delta n = n_{TM} - n_{TE} = 0.012$ compared to the c-axis films ($\Delta n = -0.027$).

The surface quality of the deposited films is good, a rms roughness of about

1 nm was measured by atomic force microscopy. The good quality of the film surface leads to low loss waveguiding. Thus, the typical value of the loss coefficient is 3 dB/cm for the c-axis films and about 4 dB/cm for the a-axis films.

Mach-Zehnder waveguide modulators were fabricated using standard lithography and ion beam etching. The waveguides are of ridge type and ensure single mode propagation in the wavelength range 633 nm - 1550 nm, having a ridge width of 2 μm and a ridge height of 70 nm.

In the case of Mach-Zehnder modulators fabricated on c-axis films, the external electric field was applied perpendicular to the optical axis of the film. An effective electro-optic coefficient of $r_{51}^{eff} = 87 \text{ pm/V}$ was measured.

The Mach-Zehnder modulators fabricated on a-axis films have a half wave voltage of $V_{\pi} = 9.5 \text{ V}$ at the fiber optic communication wavelength (1.5 μm) and a high extinction ratio of 20 dB. In this case, the driving field was applied along the optical axis and an effective Pockels coefficient r_{33}^{eff} of 42 pm/V was measured at this wavelength.

As a next step towards the integration of ferroelectric BaTiO₃ thin films on different substrates, we have modified the growth conditions by lowering the growth temperature to study polycrystalline BaTiO₃ thin films. A series of BaTiO₃ films on MgO were grown by pulsed laser deposition in order to optimize the growth parameters for low loss polycrystalline BaTiO₃ films. The films grown at a temperature of about 400 °C were polycrystalline, having an average grain size of 19 nm. They are still highly transparent, with a waveguiding loss coefficient of 4 dB/cm and a surface rms roughness of 1 nm. Mach-Zehnder waveguide modulators based on polycrystalline BaTiO₃ films were fabricated and the electro-optic response of the films was measured. A hysteretic response of the films was observed. At relatively high values of the applied electric fields (9 V/ μm) the films showed an effective electro-optic coefficient of about 22 pm/V, measured at the wavelength of fiber optic communications (1.5 μm).

List of Figures

2.1	Unit cells of the four phases of BaTiO ₃	4
2.2	BaTiO ₃ unit cell: a) cubic phase; b) tetragonal phase.	5
2.3	Temperature dependence of the cell parameters of BaTiO ₃ . V is the unit cell volume and b' , c' , V' are cell parameters of the pseudo-cubic unit cell (after Kay and Vousden [10]).	6
2.4	Temperature dependence of the refractive indices of BaTiO ₃ (after Hofmann <i>et al.</i> [12]).	6
3.1	Asymmetric planar dielectric waveguide.	9
3.2	End-fire coupling.	11
3.3	Grating coupler.	11
3.4	Retardation plate.	14
3.5	The index ellipsoid. The coordinates (xyz) are the principal axes and (n_x, n_y, n_z) are the principal refractive indices of the crystal.	15
3.6	c-axis film Mach-Zehnder modulator.	17
3.7	Output intensity of a Mach-Zehnder modulator with driving field perpendicular to the optical axis. Numerical values used for simulation: $n_o = 2.351$, $n_e = 2.330$, $r_{51} = 80$ pm/V, $\lambda = 1550$ nm, $\psi = 0$ degrees.	20
3.8	Calculated response for "push-pull" geometry, applied field perpendicular to optical axis.	21
3.9	Output intensity of a Mach-Zehnder modulator with driving field along the optical axis. Numerical values used for simulation: $n_o = 2.365$, $n_e = 2.353$, $r_{33}^{eff} = 50$ pm/V, $\lambda = 1550$ nm.	23
4.1	Sketch of a PLD-system.	26
4.2	Sketch of the four-circle x-ray diffractometry.	26

4.3	X-ray diffraction in symmetrical reflection geometry.	27
4.4	Rutherford backscattering. a) Random experiments; b) channeling experiments.	28
4.5	Atomic force microscopy: principle of operation.	29
4.6	Thin film Mach-Zehnder modulator.	31
4.7	Microscope photograph of the "Y" branch, with a fork angle of 1°	32
4.8	Microscope photograph of the cleaved edge of the modulator. .	33
4.9	Dielectric ridge waveguide. Effective index of refraction, as well as the bulk index, are indicated in the wave-guiding layer. $n'_{eff1} > n_{eff1}$	33
4.10	Simulated intensity profile of the TEM_0 mode. Ridge width is $3 \mu m$, ridge height is 70 nm	34
4.11	Fabrication of the ridge waveguides.	35
4.12	Prism coupler.	38
4.13	Prism coupling set-up for thickness, refractive index and attenuation measurements.	39
4.14	Sketch of the experimental setup for electro-optical measurements.	40
4.15	The experimental setup for frequency response measurements. .	41
4.16	RBS/ ion channeling spectra of an $1 \mu m$ thick c-axis oriented $BaTiO_3$ film on MgO	43
4.17	a) Conventional x-ray diffraction pattern of an $1 \mu m$ thick $BaTiO_3$ film on MgO (100); b) two theta scan of $BaTiO_3$ (103) at $\psi = 18.6^\circ$; c) rocking curve of (002); d) ϕ scan of (202). . .	44
4.18	AFM image of a $3 \times 3 \mu m^2$ c-axis oriented epitaxial $BaTiO_3$ film on MgO . The film thickness is $1 \mu m$, the rms roughness is 0.98 nm	45
4.19	Loss measurement for a c-axis epitaxial $BaTiO_3$ film on MgO . The loss coefficient is about 3 dB/cm	46
4.20	Response of the modulator at 633 nm wavelength. The squares are the experimental data and the line is the theoretical response with $r_{51}^{eff} = 87 \text{ pm/V}$	47
4.21	Response of the modulator at $1.5 \mu m$ wavelength.	48
4.22	Response of the modulator for $E(t)$ applied to one arm (squares), $-E(t)$ applied to the other arm (crosses) and both applied simultaneously (line). Measurements were performed at $1.5 \mu m$ wavelength.	49
4.23	Modulation vs frequency (21 V_{p-p} modulating square signal, 46 V_{dc} bias, 1550 nm light).	50
4.24	Packaged $BaTiO_3$ thin film Mach-Zehnder modulator.	51

4.25	RBS/channelling spectra of an 1 μm thick BaTiO_3 a-axis film. Minimum yield is $\chi_{min} = 1\%$	52
4.26	a) Conventional x-ray diffraction pattern of an 1 μm thick epitaxial a-axis oriented BaTiO_3 film on MgO (100); b) two theta scan of BaTiO_3 (101), (202) and (303) reflections at $\psi = 45.5^\circ$; the rocking curve of (002) peak of BaTiO_3 ; the ϕ scan of the (103) peak of BaTiO_3	54
4.27	Loss measurement for an a-axis epitaxial BaTiO_3 film on MgO	55
4.28	Performance of Mach-Zehnder modulators made from a-axis films at 633 nm wavelength.	56
4.29	Response of the a-axis modulator at 1.5 μm wavelength.	57
4.30	Photographs of the "on" and "off" states of the modulator taken with a microscope objective and a CCD camera at 1.5 μm	57
4.31	RBS spectum of a 1 μm thick polycrystalline BaTiO_3 film deposited on MgO	59
4.32	Grazing incidence XRD spectrum of as-grown polycrystalline BaTiO_3 deposited on MgO	60
4.33	AFM image of 1 μm thick polycrystalline BaTiO_3 film on MgO . Scanned area is $1 \times 1 \mu\text{m}^2$, $z = 2.5 \text{ nm/div}$	61
4.34	SEM image of 1 μm thick polycrystalline BaTiO_3 film on MgO . The sample was cleaved.	62
4.35	Loss measurement for an 1 μ polycrystalline BaTiO_3 film on MgO . The loss coefficient is about 4 dB/cm.	63
4.36	Poling and relaxation time response of a polycrystalline BaTiO_3 optical modulator.	64
4.37	Response of the modulator while changing the applied voltage at 633 nm wavelength and 1550 nm wavelength. The voltage was applied to one arm of the modulator and the electrode spacing was 10 μm	65
4.38	Response of polycrystalline BaTiO_3 modulator with 5 μm electrodes separation at 1.5 μm wavelength.	66

List of Tables

2.1	The BaTiO ₃ phases.	5
2.2	Electro-optic coefficients for single crystal BaTiO ₃ at 23 °C . .	7
3.1	Jones vectors.	13
4.1	Processes and parameters for ridge waveguides fabrication. . .	36
4.2	Processes and parameters for electrodes deposition.	37
4.3	Deposition parameters for PLD deposited c-axis and a-axis films.	52
4.4	Lattice parameters of epitaxial a-axis and c-axis oriented films on MgO in comparison with lattice parameters of bulk BaTiO ₃ .	53
4.5	The in-plane and out-of plane refractive indices of the a-axis films and c-axis films.	53

Bibliography

- [1] C. Buchal, L. Beckers, A. Eckau, J. Schubert, and W. Zander, “Epitaxial BaTiO₃ thin films on MgO,” *Materials Science and Engineering B (Solid-State Materials for Advanced Technology)* **56**, 234 (1998).
- [2] S. Thony, H. Lehmann, and P. Gunter, “Sputter deposition of epitaxial waveguiding KNbO₃ thin films,” *Applied Physics Letters* **61**, 373 (1992).
- [3] X. Lansiaux, E. Dogheche, D. Remiens, M. Guilloux-viry, A. Perrin, and P. Ruterana, “LiNbO₃ thick films grown on sapphire by using a multistep sputtering process,” *Journal of Applied Physics* **90**, 5274 (2001).
- [4] A. Boudrioua, E. Dogheche, D. Remiens, and J. Loulergue, “Electro-optic characterization of (Pb, La)TiO₃ thin films using prism-coupling technique,” *Journal of Applied Physics* **85**, 1780 (1999).
- [5] M. Blomqvist, J.-H. Koh, S. Khartsev, A. Grishin, and J. Andreasson, “High-performance epitaxial Na_{0.5}K_{0.5}NbO₃ thin films by magnetron sputtering,” *Applied Physics Letters* **81**, 337 (2002).
- [6] G. Haertling, “PLZT electrooptic materials and applications-a review,” *Ferroelectrics* **75**, 25 (1987).
- [7] M. Zgonik, P. Bernasconi, M. Duelli, R. Schlessner, P. Gunter, M. Garrett, D. Rytz, Y. Zhu, and X. Wu, “Dielectric, elastic, piezoelectric, electro-optic, and elasto-optic tensors of BaTiO₃ crystals,” *Physical Review B (Condensed Matter)* **50**, 5941 (1994).
- [8] M. B. Klein, in *Electro-optic and Photorefractive Materials*, P. Günter, ed., (Springer-Verlag, Berlin, 1986).
- [9] Y. Xu, *Ferroelectric Materials and their application* (Elsevier Science Pub. Co., Amsterdam New York, 1991).
- [10] H. Kay and P. Vousden, *Philos. Mag.* **40**, 1019 (1949).

- [11] D. N. Nikogosyan, *Properties of Optical and Laser-Related Materials* (John Wiley & Sons Inc., New York, 1997).
- [12] F. Jona and G. Shirane, *Ferroelectric Crystals* (Pergamon Press, Oxford-New York, 1962).
- [13] A. Yariv, *Optical electronics in modern communications* (Oxford University Press, New York, NY, 1997).
- [14] *Integrated Optoelectronics*, K. J. Ebeling, ed., (Springer-Verlag, Berlin, 1993).
- [15] *Fundamentals of Photonics*, B. Saleh and M. Teich, eds., (John Wiley & Sons Inc., New York, 1991).
- [16] P. K. Tien, "Light Waves in Thin Films and Integrated Optics," *Appl. Opt.* **10**, 2395 (1971).
- [17] *Integrated Optics*, R. G. Hunsperger, ed., (Springer, Berlin, 1995).
- [18] E. Voges, in *Electro-optic and Photorefractive Materials*, P. Günter, ed., (Springer-Verlag, Berlin, 1986).
- [19] A. Yariv and P. Yeh, *Optical waves in Crystals* (John Wiley & Sons, New York, 1983).
- [20] F. Abdi, M. Fontana, M. Aillerie, and G. Godefroy, "Strongly temperature dependent electro-optic coefficients in ," *Ferroelectrics* **133**, 175 (1992).
- [21] P. Ehrhart, in *Nanoelectronics and Information Technology*, R. Waser, ed., (Wiley-VCH, Weinheim, 2003).
- [22] J.-K. Heinsohn, R. Dittmann, J. Contreras, J. Scherbel, A. Klushin, M. Siegel, C. Jia, S. Golubov, and M. Kupryanov, "Current transport in ramp-type junctions with engineered interface," *Journal of Applied Physics* **89**, 3852 (2001).
- [23] J.-K. Heinsohn *et al.*, "Effect of the magnetic-field orientation on the modulation period of the critical current of ramp-type Josephson junctions," *Journal of Applied Physics* **90**, 4623 (2001).
- [24] M. Suga, M. Hiratani, C. Okazaki, M. Koguchi, and H. Kakibayashi, "Characterization of hetero-epitaxial PZT capacitor," *Integrated Ferroelectrics* **18**, 389 (1997).

- [25] A. Petraru, J. Schubert, M. Schmid, and C. Buchal, “Ferroelectric BaTiO₃ thin-film optical waveguide modulators,” *Applied Physics Letters* **81**, 1375 (2002).
- [26] B. Cullity, *Elements of X-Ray Diffraction* (Addison-Wesley Publishing Company Inc., 1978).
- [27] C. Kittel, *Einführung in die Festkörperphysik*, 12. ed. (R. Oldenbourg, München, 1999).
- [28] A. Segmuller, in *Advances in X-ray Analysis*, S. Barrett, J. Cohen, J. Faber, R. Jenkins, D. Leyden, J. Russ, and P. K. Predecki, eds., (Plenum Publishing Corp., 1986), Vol. 29.
- [29] L. Doolittle, “Algorithms for the rapid simulation of Rutherford backscattering spectra,” *Nucl. Instr. Meth.* **B9**, 344 (1985).
- [30] W. Chu, J. Mayer, and M. Nicolet, *Backscattering Spectrometry* (Academic Press, New York, 1978).
- [31] P. Ebert, K. Szot, and A. Roelofs, in *Nanoelectronics and Information Technology*, R. Wasser, ed., (Wiley-VCH, Weinheim, 2003).
- [32] A. Eckau, *Optische und elektrooptische Eigenschaften von BaTiO₃-Dünnschichtwellenleitern* (Doktorarbeit, Universität zu Köln, 2000).
- [33] H. Kogelnik, *Theory of dielectric waveguides, in Integrated optics edited by T. Tamir, 2nd edn.*, (Springer, Berlin, Heidelberg, 1979).
- [34] M. Siegert, “Private communication.”
- [35] R. Ulrich and R. Torge, “Measurement of thin film parameters with a prism coupler,” *Applied Optics* **12**, 2901 (1973).
- [36] L. Feldman, J. W. Mayer, and S. Picraux, *Materials Analysis by Ion Channeling* (Academic, New York, NY, 1982).
- [37] “JCPDS Powder Diffraction File (JCPDS International Centre for Diffraction Data),” , 1999.
- [38] D. Fork, F. Armani-Leplingrad, J. Kingston, and G. Anderson, “Thin film epitaxial oxide optical waveguides,” *Mat. Res. Soc. Proc.* **392**, 189 (1995).

- [39] L. Beckers, J. Schubert, W. Zander, J. Ziesmann, A. Eckau, P. Leinenbach, and C. Buchal, "Structural and optical characterization of epitaxial waveguiding BaTiO₃ thin films on MgO," *J. Appl. Phys.* **83**, 3305 (1998).
- [40] J. Schubert, O. Trithaveesak, A. Petraru, C. Jia, R. Uecker, P. Reiche, and D. Schlom, "Structural and optical properties of epitaxial BaTiO₃ thin films grown on GdScO₃(110)," *Applied Physics Letters* **82**, 3460 (2003).
- [41] D. Gill, C. Conrad, G. Ford, B. Wessels, and S. Ho, "Thin-film channel waveguide electro-optic modulator in epitaxial BaTiO₃," *Appl. Phys. Lett.* **71**, 1783 (1997).
- [42] B. Wessels, "Ferroelectric oxide epitaxial thin films: synthesis and non-linear optical properties," *J. Crystal Growth* **195**, 706 (1998).
- [43] V. Srikant, E. J. Tarsa, D. R. Clarke, and J. S. Speck, "Crystallographic orientation of epitaxial BaTiO₃ films: The role of thermal-expansion mismatch with the substrate," *J. Appl. Phys.* **77**, 1517 (1995).
- [44] D. Kim and H. Kwok, "Pulsed laser deposition of BaTiO₃ thin films and their optical properties," *Appl. Phys. Lett.* **67**, 1803 (1995).
- [45] T. Zhao, F. Chen, H. Lu, G. Yang, and Z. Chena, "Thickness and oxygen pressure dependent structural characteristics of BaTiO₃ thin films grown by laser molecular beam epitaxy," *Journal of Applied Physics* **87**, 7442 (2000).
- [46] C. L. Li, Z. H. Chen, Y. L. Zhou, and D. F. Cui, "Effect of oxygen content on the dielectric and ferroelectric properties of laser-deposited BaTiO₃ thin films," *J. Phys.: Condens. Matter* **13**, 5261–5268 (2001).
- [47] L. H. Robins, D. L. Kaiser, L. D. Rotter, P. K. Schenck, G. T. Stauff, and D. Rytz, "Investigation of the structure of barium titanate thin films by Raman spectroscopy," *Journal of Applied Physics* **76**, 7487 (1994).
- [48] R. Delhez, T. H. de Keijser, and E. J. Mittemeijer, "Determination of Crystallite Size and Lattice Distortion through X-Ray Diffraction Line Profile Analysis," *Fresenius Z Anal. Chem.* **312**, 1–16 (1982).
- [49] P. Van Buskirk, R. Gardiner, and P. Kirlin, "Plasma-enhanced metalorganic chemical vapor deposition of BaTiO₃ films," *Journal of Vacuum Science & Technology A (Vacuum, Surfaces, and Films)* **10**, 1578 (1992).

-
- [50] D. Gill, B. Block, C. Conrad, B. Wessels, and S. Ho, “Thin film channel waveguides fabricated in metalorganic chemical vapor deposition grown BaTiO₃ on MgO,” Appl. Phys. Lett. **69**, 2968 (1996).

Acknowledgments

Finally, I want to thank everybody who helped and supported me during this work. My special thanks go to:

Prof. Dr. Christoph Buchal

First of all, I would like to thank to my wonderful professor who gave me the chance to work at this thesis. He has supported me all the time from the very beginning. He is for me a real model as a scientist as well as in private life. He has done so many things for me and I have learnt a lot from him, during many hours of useful discussions. He has showed me enthusiasm and he has guided me with much patience to carry out my research work at FZJ. Every time when I was in need, he was the one who gave me a hand and showed me affection.

Prof. Dr. Ladislav Bohatý

I thank warmly Prof. Bohatý for his support within "Graduiertenkolleg - Azentrische Kristalle". He gave me the wonderful opportunity to participate at many of his interesting courses and presentations regarding physics of crystals. I am also very thankful to him that he accepted to be part of the final commission.

Prof. Siegfried Mantl and Prof. Lüth

I would like to thank Prof. Mantl and Prof. Lüth for giving me the opportunity to carry out my research work at Forschungszentrum Juelich.

Dr. Jürgen Schubert

My special thanks go to my experienced colleague who helped me a lot in my work from the very beginning with his catching enthusiasm and energy. Besides many long and constructive discussions regarding my research, he has grown many samples that I used during this work.

Dipl. Phys. Martin Schmid

I thank him for the huge amount of samples he has grown for me. He is also a very dear friend to me and we spent a very good time together at different conferences as well as in private life.

Dipl. Phys. Opas Trithaveesak

Special thanks to him for x-ray measurements he made for my work and a

lot of useful discussions about the structural characterization of our films.

Dr. Dan Buca

My friend and my companion from my home country introduced me to the clean room work and helped me for an easier contact to my new colleagues. Many times he helped me with his experience to solve a lot of administrative problems. We made many trips spending a very good time together. For all I thank him dearly.

Dr. Arne Eckau

I thank him for being the first person who introduced me in the experimental work on thin film optical devices.

Dr. Markus Siegert

I thank him for being the one who introduced me in the waveguide simulation programs and having with him many useful scientific discussions.

Dr. Patrick Kluth and Dr. Qing-Tai Zhao

I would like to thank Qing-Tai and Patrick for giving me useful advise for operating the clean room facilities. They instructed in the fine art of lithography. I would like to thank them for their help as well as their enthusiasm and friendship.

Dr. Stephan Winnerl

With his special warmth he became my first friend from here. I will always remember the gorgeous night when we looked at the sky through his telescope and all the biking trips made together.

Dipl. Phys. Eduard Rije

I would like to thank Eduard for his friendship as well as for his support on the special occasion of the birth of my son.

Dipl. Phys. Christian Ohly

I thank him for the SEM measurements he made for my work.

Frau Susanne Bippus and Frau Brigitte Modolo

Our secretaries, many thanks for their friendliness, efficiency and for ironing-out many administrative difficulties.

Mr. Andre Dahmen

Thanks to him I have always benefited of the newest software that is so necessary for the data analysis.

Dipl.-Ing. A. Steffen and Mr. Jürgen Müller

They thankfully maintained the clean room facility in an immaculate condition. We are all very grateful for their support.

Special thanks go to *Mrs. Mona Nonn* for lithography masks fabrication.

Frau Gisela Buchal is a very special lady for me who has always supported me and my family with her warmth and kindness.

Last, not least, my thanks go to my wife Diana. She has supported me with her love all this time and she gave me the most beautiful gift: our son, Christian Ioan.

List of Publications

Publications in refereed journals

- *Ferroelectric BaTiO₃ thin-film optical waveguide modulators*
A. Petraru, J. Schubert, M. Schmid, and Ch. Buchal
Applied Physics Letters **81**, 1375 (2002).
- *Structural and optical properties of epitaxial BaTiO₃ thin films grown on GdScO₃(110)*
J. Schubert, O. Trithaveesak, A. Petraru, C. Jia, R. Uecker, P. Reiche, and D. Schlom
Applied Physics Letters **82**, 3460 (2003).
- *Optical waveguiding in magnetron-sputtered Na_{0.5}K_{0.5}NbO₃ thin films on sapphire substrates*
M. Blomqvist, S. Khartsev, A. Grishin, A. Petraru, and Ch. Buchal
Applied Physics Letters **82**, 439 (2003).
- *An integrated optical Mach-Zehnder modulator based on polycrystalline BaTiO₃*
A. Petraru, J. Schubert, M. Schmid, O. Trithaveesak, Ch. Buchal
Accepted for publication to Optics Letters.
- *Ferroelectric BaTiO₃ Thin Film Optical Waveguide Modulators*
A. Petraru, M. Siegert, M. Schmid, J. Schubert, and Ch. Buchal
Mat. Res. Soc. Proc. 688 (2002).

Contributions to conferences

- *Epitaxial and Polycrystalline Ferroelectric BaTiO₃ thin films used for optical switching*

Poster presentation at 11th European Conference on Integrated Optics, Prague, April 2 - 4, 2003.

- *Electro-optic Mach-Zehnder modulators based on polycrystalline BaTiO₃ thin films on MgO*

A. Petraru, J. Schubert, M. Schmid, and Ch. Buchal

Oral presentation at the Frühjahrstagung der DPG, Dresden, March 24 - 28, 2003

- *Ferroelectric BaTiO₃ thin film optical waveguide modulators*

A. Petraru, M. Schmid, J. Schubert, Ch. Buchal

Poster presentation at 3rd Rigi Workshop, 1st - 5th August 2002

- *Ferroelectric BaTiO₃ Thin Film Optical Waveguide Modulators*

A. Petraru, J. Schubert, M. Schmid, Ch. Buchal

Poster presentation at the Frühjahrstagung der DPG, Regensburg, March 11 - 15, 2002

- *Ferroelectric BaTiO₃ Thin Film Optical Waveguide Modulators*

A. Petraru, M. Siegert, M. Schmid, J. Schubert, and Ch. Buchal

Poster presentation at the MRS Fall Meeting, Boston, November 26-30, 2001.

- *An Electrooptical BaTiO₃ thin film waveguide modulator*

A. Petraru, M. Siegert, A. Eckau, M. Schmidt, J. Schubert and Ch. Buchal

Oral presentation at 10th European Conference on Integrated Optics, Paderborn, April 4 - 6, 2001

Curriculum Vitae

Personal data

Name	Petraru
First name	Adrian Ion
Birth date	4 January 1970 in Braila
Country	Romania

Education

09/1976-07/1980	Elementary school in Braila
09/1980-07/1984	Gymnasium in Braila
09/1984 - 07/1988	Lyceum "Nicolae Iorga", Braila Lyceum diploma: Bacalaureat (Abitur)
10/1989-06/1994	Faculty of Physics, University of Bucharest Department of Electronic Physics
July 1994	Graduated in Physics Final exams grade: 8.92/9.66 Graduate thesis: <i>Frequency synthesis</i> Title: Dipl. Phys.
08/2000 - 08/2003	Ph.D student at Köln University Subject: <i>Optical and electro-optical properties of BaTiO₃ thin films and Mach-Zehnder waveguide modulators</i>

Work experience

10/1994 -8/2000	Scientific co-worker at Solid-State Quantum Electronics Department, National Institute of Laser Plasma and Radiation Physics Bucharest
-----------------	---

Erklärung

Ich versichere, daß ich die von mir vorgelegte Dissertation selbständig angefertigt, die benutzten Quellen und Hilfsmittel vollständig angegeben und die Stellen der Arbeit - einschließlich Tabellen, Karten und Abbildungen-, die anderen Werken im Wortlaut oder dem Sinn nach entnommen sind, in jedem Einzelfall als Entlehnung kenntlich gemacht habe; daß diese Dissertation noch keiner anderen Fakultät oder Universität zur Prüfung vorgelegen hat; daß sie abgesehen von unten angegeben Teilpublikationen noch nicht veröffentlicht worden ist sowie, daß ich eine solche Veröffentlichung vor Abschluß des Promotionsverfahrens nicht vornehmen werde. Die Bestimmungen dieser Promotionsordnung sind mir bekannt. Die von mir vorgelegte Dissertation ist von Herrn Prof. Buchal betreut worden.